Nanoscale tribological studies of friction and wear on graphitic surfaces

Dissertation

zur Erlangung des akademischen Grades
des Doktors der Naturwissenschaften
an der Naturwissenschaftlich- Technischen Facultät II
-Physik und Mechatronik-
der Universität des Saarlandes

von

Balakrishna Soorali Ganeshamurthy M.Sc

Saarbrücken

2015

Tag des Kolloquiums:	30.07.2015
Dekanin/Dekan:	Univ.-Prof. Dr.-Ing. G. Frey
Mitglieder des Prüfungsausschusses	Univ.-Prof. Dr. R. Pelster (Vorsitzender)
	Prof. Dr. R. Bennewitz
	Univ.-Prof. Dr. U. Hartmann
	Dr. F. Müller

Dedication

This thesis is dedicated to my beloved parents Nagarathna Soorali,

Ganeshamurthy Soorali and to all my teachers who greatly shaped my life.

Eidesstattliche Versicherung

Hiermit versichere ich an Eides statt, dass ich die vorliegende Arbeit selbstständig und ohne Benutzung anderer als der angegebenen Hilfsmittel angefertigt habe. Die aus anderen Quellen oder indirekt übernommenen Daten und Konzepte sind unter Angabe der Quelle gekennzeichnet. Die Arbeit wurde bisher weder im In- noch im Ausland in gleicher oder ähnlicher Form in einem Verfahren zur Erlangung eines akademischen Grades vorgelegt.

Ort: _____

Datum: _____

Unterschrift: _____

Contents

ABSTRACT

Understanding the atomistic origin of friction forces helps to design more efficient mechanical systems and lubricants. Atomic Force Microscopy (AFM) is a powerful tool for measuring mechanical properties in field of surface science. AFM, beyond imaging the surfaces at nanoscale, can also probe the surface forces down to piconewton forces and thus contribute to our understanding of friction at the atomic scale. In this thesis we present the results of AFM investigations into nanoscale friction anisotropy on graphitic materials and into the mechanical strength of graphene on Pt(111). We have discovered that on graphitic surfaces the friction forces reveal preferred sliding directions. Any deviation from the preferred directions results in a transverse component of friction which forces the slider to move along one of one of the atomic zigzag directions. For sliding on graphene/Pt(111) with increasing load we found three distinct regimes. At very low loads, sliding is entirely elastic and the friction is almost negligible. As load is increased, the platinum substrate undergoes plastic deformation but the graphene layer is unaffected. At very high pressures ($>$ 50GPa) graphene ruptures and loses its protective character.

Das Verständnis der atomaren Grundlagen der Reibung trägt zum Design effizienterer mechanischer Systeme und Schmiermittel bei. Das Atomic Force Microscope (AFM) ist ein wichtiges Instrument für die Bestimmung mechanischer Eigenschaften in den Oberflächenwissenschaften. Über die Abbildung von Oberflächen auf der Nanoskala hinaus vermag es, Kräfte mit Piconewton-Auflösung zu bestimmen und damit das Verständnis der Reibung auf atomarer Skala zu verbessern. In dieser Arbeit stellen wir die Ergebnisse einer AFM-Untersuchung zur Reibungsanisotropie auf graphitischen Oberflächen und zur mechanischen Haltbarkeit von Graphen auf Pt(111) vor. Wir haben entdeckt dass Reibungskräfte bevorzugte Gleitrichtungen auf graphitischen Oberflächen anzeigen. Jede Abweichung von der Vorzugsrichtung führt zu einer transversalen Komponente der Reibungskraft, die ein Gleiten entlang einer der sechs atomaren Zickzack-Richtungen bewirkt. Für das Gleiten auf Graphene/Pt(111) mit zunehmender Auflagekraft haben wir drei Bereiche fest-

gestellt. Bei niedrigen Auflagekräften erfolgt das Gleiten vollständig elastisch und die Reibung ist vernachlässigbar klein. Mit zunehmender Last wird das Platin plastisch verformt während der Graphenfilm intakt bleibt. Bei hohen Drücken (>50GPa) reißt das Graphen und verliert seine Schutzwirkung.

Part I.

Introduction

1. Introduction

The work presented in this thesis is related to the tribological characteristics of graphene explored with the help of an Atomic Force Microscope (AFM). The chapters are grouped into four parts. The first three parts contain literature reviews related to their respective topics. The first part introduces Atomic Force Microscopy, its historic development and working principle. The second part explains our work on anisotropic friction forces on graphitic surfaces. In this part we introduce the the measurement technique of Cartesian components of friction force using an AFM. The third part of this thesis describes the work on mechanical properties of graphene epitaxially grown on Pt(111). Here we show the preparation method of graphene on Pt(111) and the briefly report on simulation results of nanoscratch tests by our collaborators. Then we show our experimental verification of the simulation results and discuss the results. The final part of this thesis is dedicated to the conclusions and outlook drawn from our work.

1.1. General idea and role of nanotribology

The word *tribology* was coined by Peter Jost in 1966. It has its origin in the Greek word τριβ which means *"to rub"*. Tribology is mainly concerned with experimental and theoretical investigations of processes of friction, lubrication and wear. Leonardo da Vinci (1452–1519) was the first to study concepts of friction. According to da Vinci, the frictional resistance scales with the load applied but is independent of the contact area. Later Guillaume Amontons extended the findings of da Vinci. He investigated the origins of frictional force and he attributed them to the roughness of

two contacting surfaces. Adhesion effects were not considered at that time. Amonton's theories were further developed by Charles-Augustin de Coulomb (1785) who stated the law of velocity dependent friction. The two regimes observed for friction are *static friction* and *kinetic friction* between two moving surfaces or contacts. It is governed by the model

$$F_{\mathrm{f}} = \mu F_{\mathrm{n}} \tag{1.1}$$

where F_{f} can have values between zero and μF_{n}.

F_{f} is the friction force parallel to the interacting surfaces and opposite to the direction of motion, μ is the coefficient of friction, which is an empirical quantity related to the contacting materials, F_{n} is the normal force exerted by each other and is directed perpendicular to the surface.

Later Bowden and Tabor introduced a modern concept of friction. The outcome of their systematic tribological studies showed that the contact of between two macroscopic bodies is formed by numerous small asperities, i.e. the apparent contact area is different from the real contact area. The real contact area is a sum of multiple contact zones of contact area a_i, therefore the total real contact area of A_R=$\sum a_i$. According to this model friction is proportional to both the real area A_R and mean lateral force per unit area,which is shear strength τ.

$$F_R = \tau \times A_R \tag{1.2}$$

Here F_R is the friction force measured, τ is called shear strength which is related to the fundamental property of the interface and A_R is real area of contact. Much about the shear strength τ is unknown. Number of contacting asperities and the real contact area increases when the applied load is increased. The contact radius can be determined with the Hertz theory assuming that the real contact area due to asperities is much smaller than the radius of curvature of the asperity, R.

$$a^3 = \frac{3PR}{4E^*} \tag{1.3}$$

$$E^* = (\frac{1 - v_1^2}{E_1} + \frac{1 - v_2^2}{E_2}) \tag{1.4}$$

where E_i and v_i represent the Young's modulus and Poisson ratio, respectively, for the two surfaces in contact and P is the load applied.

The friction scales linearly with number of asperities. Therefore it is convenient to denote shear strength σ as lateral force per area $(\frac{F_L}{A_R})$

$$\sigma = \frac{F_L}{A_R} \tag{1.5}$$

σ has the dimension of a pressure. Generally the the relation between the load (P) and shear strength σ is defined as,

$$\sigma = \sigma_0 + \alpha P \tag{1.6}$$

where σ_0 is a constant and P is the normal load per unit area. From equation 1.5 it follows that

$$F_L = (\sigma_0 + \alpha P)A_R \tag{1.7}$$

$$= (\sigma_0 + \alpha \frac{F_N}{A_R})A_R \tag{1.8}$$

$$= \sigma_0 A_R + \alpha F_N \tag{1.9}$$

When the normal pressure P becomes large compared to σ_0 equation 1.9 reduces to Amonton's law of friction $F_L \approx \alpha F_N$.

The problem of friction and wear in nanotribology, reduces to the study of how asperities interact between the sliding surfaces. Hence tribological study at the mi-

cro and nano scales gains importance in order to completely understand the friction and wear process. Microelectromechanical systems (MEMS)/nanoelectromechanical systems (NEMS), such as disk drives, storage systems and the miniaturization mechanical devices are posing new tribological challenges and there is a need of developing mechanically stable solid lubricants which also show a very low friction and adhesion

Understanding atomistic origins of friction and wear is of crucial importance in understanding the macroscopic level friction and wear processes. Nanotribology is the subfield of tribology which studies the tribological phenomena at the nanoscale. The Atomic Force Microscope is a very useful tool to explore the surface interactions at the small scales down to few nanometers. Nanotribological studies are helping to understand the fundamental mechanisms of friction and wear phenomena thereby helping in designing energy efficient long lasting devices.

1.2. Role of graphite in tribology

Graphite is composed of planes of polycyclic carbon atoms. The bonding between adjacent layers is weak therefore the distance between the layers is larger compared to the interatomic distance of carbon atoms (see figure.1.1). The molecular planes in graphite are very easy to shear. Graphite is thermally very stable and can withstand at higher temperatures. This makes graphite a good solid lubricant. Graphite is well suited for lubrication in a ambient atmosphere. Reactive dangling covalent edge sites of graphite are passivated by the adsorption of water, due to which atomic planes in the graphite shear easily. But in vacuum and dry environments graphite exhibits high friction. Therefore graphite in presence of water is a good lubricant [69]. Several research groups have studied the frictional properties of highly oriented pyrolytic graphite with the help of Atomic Force Microscope [51, 66, 65].

Graphene is a single layer of graphite. The discovery of graphene in 2004 by mechanical exfoliation of graphite using scotch tape opened up a new era of graphene research [54]. It was thought before that such a 2D materials cannot exist because of

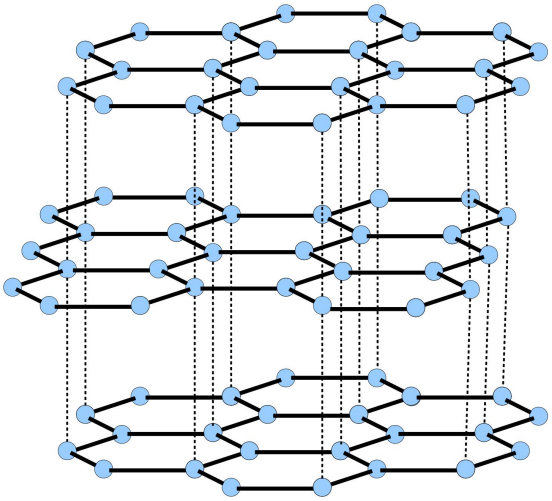

Figure 1.1.: Lamellar structure of graphite

physical instability. Apart from its well-established thermal, electrical, and mechanical properties, graphene can serve as a solid lubricant. Its high chemical inertness, easy shearing and mechanical stability make it an attractive candidate for nanoscale lubrication. Graphene's extreme toughness suppresses the material wear as surface protective coating. Graphene being impermeable to gas and liquids, so it is a good candidate as material for anti-corrosive coating. All these properties make graphene very attractive for tribological applications. Even the multilayer graphene is ultra-thin, it is best suited for nano-scale or micro-scale mechanical systems such as microelectromechanical systems (MEMS) and nanoelectromechnical systems (NEMS). Graphene's mechanical stability when used as a lubricant under very high loading pressures is still an open question. Usability of graphene as a solid lubricant or an additive to liquid lubricant are still open for research. Methods for preventing the wear of graphene coating itself have to be discovered. The stability depended on the size of asperity of the interacting surface and the load as well. In our study we have focused on the experimental verification of graphene's higher mechanical stability and wear protective action deduced from the simulation results.

2. Atomic force microscopy

Advancements in nanotechnology and miniaturization of mechanical and electrical devices demands a profound understanding of the atomic interactions and tribological properties at the nanoscale. In recent years, Atomic Force Microscopy (AFM) has become a powerful tool, sensitive enough, probe forces down to Piconewton. Atomic manipulation and investigations into the origins of friction and wear mechanisms are possible with the help of an AFM. An AFM operates on a different principle than other microscope, such as electron microscope or optical microscope. It operates by detecting inter atomic forces using a cantilever in the AFM that bends in response to forces that experienced when it hovers very close or in contact with the surface.

2.1. Intermolecular and interatomic forces

The origin of the surface forces are found at the atomic level. Molecular or even macromolecular forces arise from atomic interactions. Consider diatomic molecule formed by two atoms with mass m_A and m_B. The molecular vibrational frequency ν aids the estimation of force between the two atoms. In the case of the harmonic oscillator approximation, the frequency of vibration of the molecular system is given by

$$\nu = \frac{1}{2\pi}\sqrt{\frac{k}{m_r}}$$

where k is the spring constant of the system and $m_r = \frac{m_a m_b}{m_a + m_b}$ is the reduced mass of the molecule. We briefly discuss types of major interaction between the atoms

and molecules.

- Van der Walls (short range V $1/r^6$, weak ~0.01-0.1 eV)
- Ionic (long range, V~1/r, strong ~5-10 eV)
- Metallic
- Covalent (~3 eV)

Van der Waals forces *Van der Waals forces* include attractions and repulsions between atoms, molecules, and surfaces, as well as other intermolecular forces.These forces are weaker compared to ionic, covalent or metallic bonds. The origin of vdW forces is generally ascribed to electromagnetic forces and one distinguishes three different types of contributions: the electrostatic contributions, the induction contributions and the dispersion contributions.is the sum of the attractive or repulsive forces between molecules or between parts of the same molecule other than those due to covalent bonds, or the electrostatic interaction of ions with one another, with neutral molecules, or with charged molecules. This includes force between two permanent dipoles (Keesom force) force between a permanent dipole and a corresponding induced dipole (Debye force) and force between two instantaneously induced dipoles (London dispersion force).

Ionic bonding The ionic interaction is electrostatic attraction between oppositely charged ions. Due to the difference in electronegativity, attraction occurs between the two ions to reach one the stable configuration of the closest noble gas. The high energy of the ionic bonds makes ionic solids a high melting point. A larger difference in the electronegativity between the atoms induces a stronger ionic bond.

Metallic bonding In the metallic bonding is the electrostatic attractive force that occurs between conduction electrons and positively charged metal ions.electrons move freely in the crystal. The result of having free electrons in the solid is a high thermal and electrical conductivity. As the positive ions are not directly bound

to each other, but owe their cohesion to their interactions with the valence electrons, the atoms or layers are allowed to slide past each other, resulting in the characteristic properties of malleability and ductility of metals. High melting or boiling points of metals is due to the strong attractive force between the electrons and the positive ions in metals.

2.2. Atomic Force Microscopy-Working principle

With the help of an AFM the atomic resolution and measurement of forces down to the nano Newton are possible. In 1986, Binnig and Quate demonstrated for the first time the ideas of AFM [8], which used an ultra - small probe tip at the end of a cantilever. In contrast to the STM, the AFM is not restricted to only conductive surfaces and it can be used in different environments like ultra high vacuum, ambient conditions and in liquids, to study any kinds of surfaces, including biological samples. AFM has become the popular tool for probing surfaces. The working principle of an AFM can be broadly divided into three parts. A force-sensing system, a detection system and a positioning system, all the three units are controlled by electronic feedback systems, which are usually realized with the help of a computer[1]. A schematic diagram of the AFM setup is shown in figure 2.3

2.2.1. The force-sensing system

The force-sensing system is the AFM part in direct interaction with the sample surface. A cantilever housing a sharp tip which is ideally terminated by a single atom and facing towards the sample surface, is used as sensor (figure 2.1). The tip is usually silicon or silicon nitride having a tip radius of curvature in the order of few nanometers. The AFM tip is the component in contact or in near contact with the surface. The forces between the tip and the sample surface lead to a deflection of the cantilever according to Hooke's law. Depending on the forces, and the direction of cantilever movement, there will be a torsion and/or a bending of the cantilever while scanning on a surface.

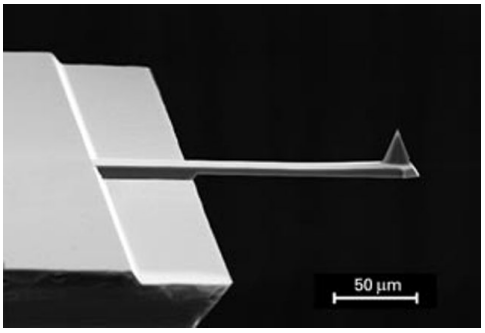

Figure 2.1.: AFM cantilever with a sharp tip at its free end that is used to probe the sample surface.

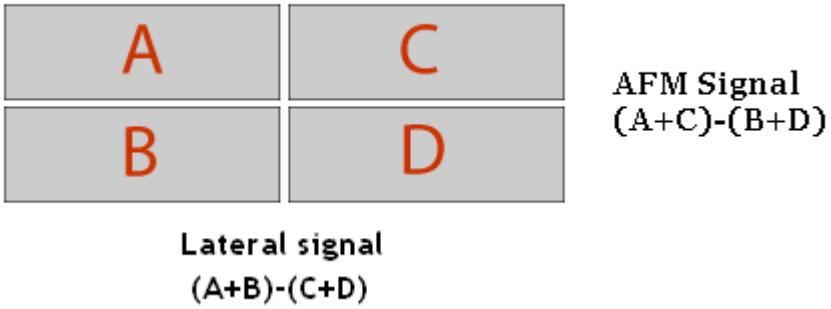

Figure 2.2.: Four quadrant photodiode detector.

2.2.2. The detection system

The interaction between tip and the sample is detected by observing the deflection of the cantilever. The most common method employed for the detection of cantilever deflection is by an optical beam deflection system [52]. A laser beam is focused onto the upper side of the cantilever and reflected back on a position detector four-quadrant position sensitive photodetector (PSPD)figure 2.2. Bending and torsion of the cantilever result in the motion of the reflected laser spot on the photodetector and thus, produces changes in the output voltage of the photodiode.

The length of the cantilever is a few hundred micron, while the thickness is only a few microns, so very small force is enough to bend or twist the cantilever. In the beam deflection scheme, bending or torsion of the cantilever is magnified since the distance between the cantilever and the photo-detector is orders of magnitude greater the length of the cantilever. Small variations in the position of the cantilever

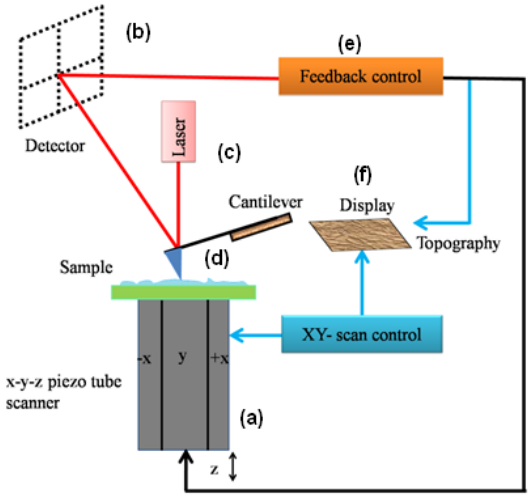

Figure 2.3.: Schematic diagram of all the three units of an AFM. (a) is a piezo tube scanner. (b) is position detector a four-quadrant position sensitive photodetector (PSPD). (c) Laser source and (d) is the cantilever probes the surface and from which the laser is reflected onto the photodiode. (e) feedback electronics which takes the voltage changes observed at the PSPD as input and converts it into images at (f).

results in large displacements of the laser spot. therefore tip displacements smaller than 1 nm are also detectable. The cantilever displacements or the forces acting on the cantilever are then measured via PSPD output voltage, provided that the photo diode sensitivity and the cantilever spring constants are known. One advantages of the detection system is its ability to record the deflection of the cantilever in the three dimensions separately and simultaneously.

2.2.3. Positioning system

Precise positioning of the AFM tip on the sample surface is done by employing piezoelectric scanners as positioning devices, whereas coarse displacements are done with the help of stepper motors. The relative position of the tip over the sample is thus controlled by the application of voltage to the electric contacts of the piezo, resulting in extension, or bending of the piezoelectric material. Piezoelectric scanners can be designed to move in the three dimensions by expanding in some directions and contracting in others. Two variations are possible, which are, tip scanning and sample scanning. For the scanning movement, either the sample or the tip can be

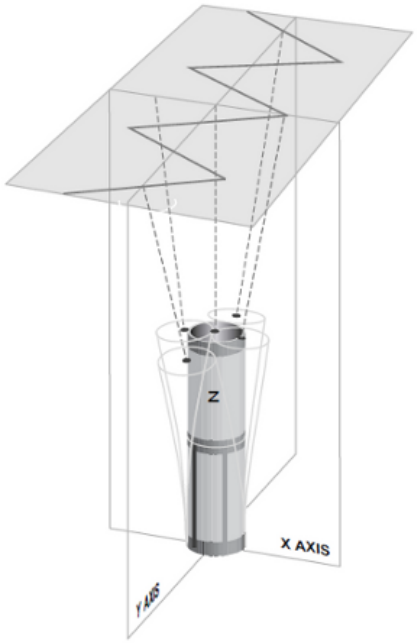

Figure 2.4.: Scanning path on a surface. The piezo tube moves from one end of the scan frame to the other end in a zigzag path collecting the data from each line.
(Image courtesy : A Practical Guide to Scanning Probe Microscopy SPM-Veeco)

moved in the first case it is a *tip scanner*; in the latter is a *Sample Scanner.*

Scanning Probe Microscopes (SPM) generate an image of the sample surface by scanning back and forth, line by line, probing the surface and collecting data. A schematic diagram of the scanner motion during data acquisition figures in figure 2.4. The laser beam is reflected on the back side of the cantilever into the four-quadrant photodetector. The intensity difference between the upper and lower segments of the four-quadrant photodetector (PSPD) is proportional to the normal deflection $I(A+B)-I(C+D)$ topography and corresponds to a change ΔV_N of the output voltage of the PSPD, whereas the intensity difference between the left and right segments is proportional to the torsion of the cantilever $I(A+C)-I(B+D)$ torsion or lateral force and is related to a PSPD output voltage variation ΔV_L.

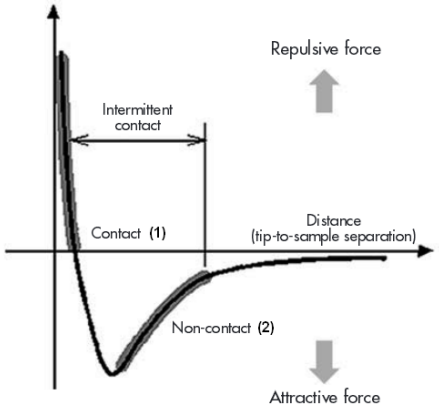

Figure 2.5.: Typical force distance curve showing attractive and repulsive regimes according to the separation distance between the tip and the surface. The contact regime (1) and (2) the non-contact regime. In the contact regime, the cantilever is held less than a few angstroms from the sample surface, and the interatomic force between the cantilever and the sample is repulsive. In the non-contact regime, the cantilever is held on the order of tens to hundreds of angstroms from the sample surface, and the interatomic force between the cantilever and sample is attractive due to the long-range *van der Waal*s interactions. (Image courtesy : A Practical Guide to Scanning Probe Microscopy SPM-Veeco)

2.3. The force-distance curve

A cantilever, experiences attractive and repulsive forces as the AFM tip is brought close to the sample surface and then pulled away. Theses forces separates two domains where an AFM can operate: the contact mode and the non-contact mode. The dependence of this force as function of the separation distance between the tip and the surface is illustrated in figure 2.5. This so-called force-distance (FD) curve is important to determine the optimum settings for the interaction between the studied surface and the AFM probe.

2.4. Modes of operation

The AFM can work in different modes depending on kinds of measurements we are interested and as well as the nature of the surface under study. Very soft and sensitive surfaces require low normal forces or even no contact between the tip and

the surface, whereas hard surfaces withstand high normal loads without damaging the surface can be scanned in contact mode.

2.4.1. Contact mode

In contact mode, the tip is slid across the surface in repulsive regime. Topography and the friction on the surface is measured either using the deflection of the cantilever directly or, using the feedback signal required to keep the cantilever at a constant height. The AFM can be operated in constant force mode or constant height mode. In the constant force mode, the force between the tip and the surface is simultaneously measured and kept constant via feedback electronics which controls vertical deflection of the cantilever. Thus, the scanner responds instantaneously to surface morphology by keeping the cantilever deflection constant. By this way, the topography is deducted from the voltage applied to the z-piezo and the scanning speed is limited by the time response of the feedback loop. In constant height mode, deflection measured from the PSPD is directly used to generate the topography image of the sample. This mode is restricted to flat surfaces to avoid tip crashes on the surface.

2.4.2. Lateral Force Microscopy

Lateral force microscopy (LFM) is relays on measuring the torsional deflection of the cantilever when the tip slides on the surface. The magnitude of this deflection is depends on the frictional coefficient. Here the AFM operates in contact mode, keeping the normal force constant and recording the torsion of the cantilever. Thus vertical and lateral bending of the cantilever are simultaneously measured. The lateral bending (or twisting) arises from forces parallel to the plane of the sample surface and acting on the AFM-tip. This lateral force has actually two main origins: first, the friction force, that is opposed to the tip displacement, and secondly, the changes in the topography. The figure 2.6 illustrates by two types the lateral force generated by a change in local slope and by a change in the friction coefficient.

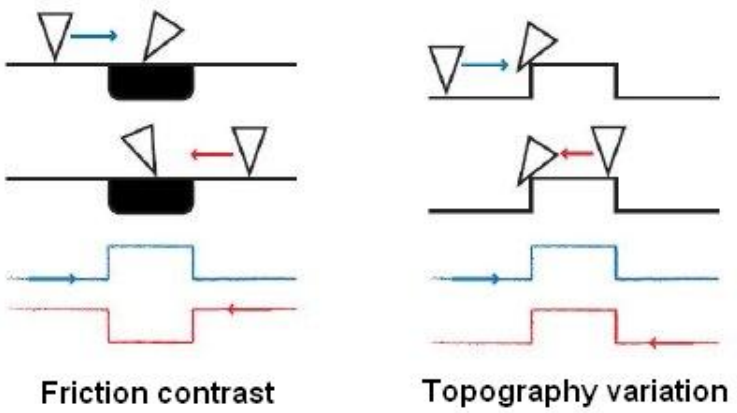

Figure 2.6.: Sketch of the lateral deflection of the cantilever induced by local changes of the friction on the surface (on the left), or coming from topography variations (on the right).

The sign of the friction force signal depends on the scan direction. The friction force signal changes its sign when the scanning direction is reversed, while the normal force remains unchanged. In fact, one scan line in the forward and reverse direction forms a loop called a friction loop figure 2.7.The total energy dissipated in the one complete cycle of sliding is given by the area enclosed by the friction loop. At the beginning sliding, the friction loop shows a linear increase of the lateral force as function of the support position (I). This is due to the static friction, the tip stick to the surface but does not move but bends until the distance moved by the piezo overcomes the restoring force in the cantilever the the tip starts to slide over the surface. The tip begins to slip (II) until the scan direction is changed and the process repeated (III $\rightarrow$ IV). The difference between the mean lateral force for the forward and backward directions corresponds to twice the mean friction force.

To exactly quantify the friction force we must calibrate the system. The lateral force excreted on a sliding tip can be calculated from the known parameters like the spring constant of the cantilever, dimensions of the cantilever,bsnsitivity and the output at the photodiode. The load applied on the surface in repulsive contact regime (F_N) and lateral force or the friction force (F_L) are given by

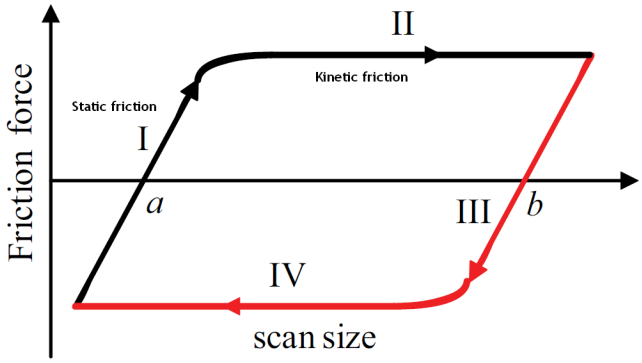

Figure 2.7.: Schematic diagram of a friction loop

$$F_N = k_N S \times V_{a-b} \tag{2.1}$$

$$F_L = \frac{3h}{2l} k_l \times S \times V_{c-d} \tag{2.2}$$

where k_N is the normal spring constant, k_l is the torsional spring constant, Both normal and torsional spring constants are calculated by the geometrical method. S is the photodetector sensitivity,V_{a-b} is the photodetector deflection signal, V_{c-d} is the photodetector lateral signal, and h is the height of the tip, and l is the length of the cantilever [50]. The sensitivity of the photodetector is measured from a force-distance curve. Force-distance curves are obtained by pressing the cantileve against the sample surface. Starting from far from the sample without the contact, tip is moved towards the surface and then slowly pressed against the surface.. Then slowly retracting the cantilever away from the surface. The sensitivity of the photodetector was determined from the slope of the cantilever deflection in response to the known distance traveled by the piezo after the cantilever tip goes into contact with the surface. The recorded deflection signal showes the linear bending of the cantilever. A hard sample surface is ideal for the force-distance measurement so that any plastic

deformation of the surface is prevented. The normal and lateral spring constant of all cantilevers were calculated by the geometrical method and are given by

$$k_N = \frac{Ewt^3}{4l^3} \tag{2.3}$$

$$k_l = \frac{Gwt^3}{3h^2l} \tag{2.4}$$

where E is the elastic modulus of the material of the cantilever, w is the width of the cantilever, t is the thickness of the cantilever, and G is the shear modulus of the material of the cantilever. Considering to the strong effect the thickness of the cantilever has on the spring constant, the average thickness of the cantilever was determined from the first normal resonant frequency of the cantilever (f_0), is given by

$$t = \frac{4\sqrt{3\pi l^2}}{1.8732} f_0 \sqrt{\frac{\rho}{E}} \tag{2.5}$$

where ρ is the density of the cantilever.

2.4.3. Non-contact mode

In the non-contact mode (NC-AFM), the cantilever is oscillated very close to the surface. The spacing between the tip and the sample in this mode is on the order of few nanometers. A stiff cantilever is attached to a small piezo ceramic system, which vibrates normally to the surface at a frequency close to the cantilever resonant frequency. [2]. In this mode, the tip is approached to the surface by oscillating the cantilever at its resonance frequency f_0. Upon close approach of the tip to the surface, the resonance frequency is shifted due to the interaction of the tip with the surface

The distance between the sample and the AFM tip is controlled by tracking the changes in the oscillating frequency, amplitude or phase.NC-AFM is desirable because it allows measuring sample topography with little or no contact between the

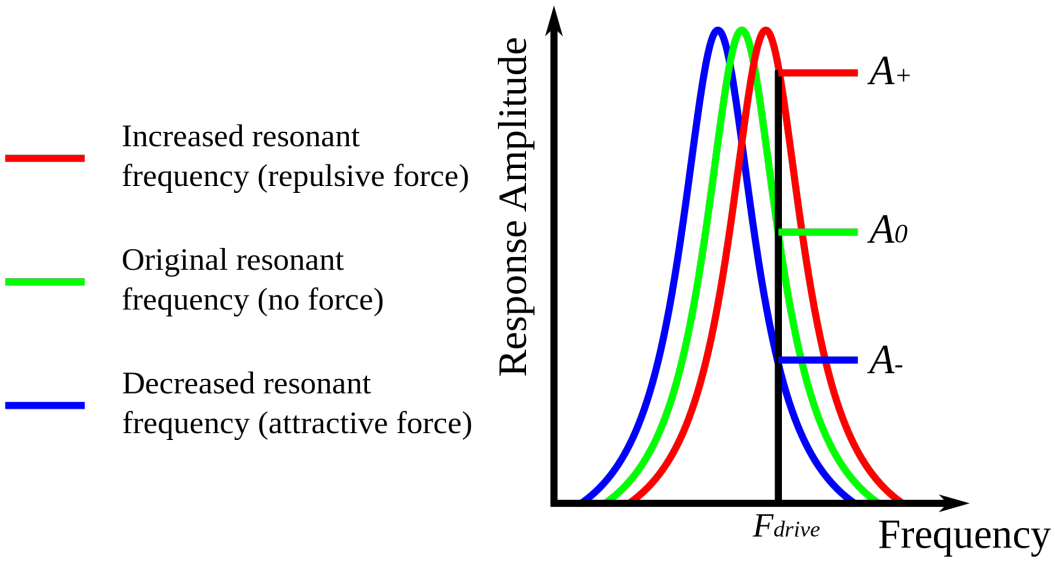

Figure 2.8.: Change ind the resonance frequency the amplitude of an oscillating cantilever due to the interaction with the surface and the tip. (Image source : wikipedia.org/wiki/Non-contact_atomic_force_microscopy)

tip and the sample. The resonance frequency shift Δf of the cantilever oscillation is a measure of the forces acting between the tip and the surface. Considering thermal excitation as the source of fluctuations limiting the detection, the minimum detectable force gradient δF_{min} is defined via the minimum detectable frequency shift δf as,

$$\delta F_{min} = \frac{2k\delta f}{f_0} = \sqrt{\frac{4kk_BTB}{\pi Q f_0 A^2}}$$

where kB, T, A and B are the Boltzmann constant, temperature, oscillation amplitude and detection bandwidth, respectively, k is the spring constant of the cantilever and Q its quality factor. It is evident that using high- Q cantilevers improves the force sensitivity in a non-contact atomic force microscope. The resonance frequency or the oscillating amplitude is kept constant by a feedback loop, which controls the cantilever displacement normal to the surface. Thus, the resonance frequency of the cantilever is indirectly used to measure the surface topography. The amplitude of cantilever oscillation is kept constant by a feedback loop, which controls the cantilever displacement normal to the surface. Thus, the resonance frequency of the

cantilever is indirectly used to measure the surface topography. Since it is possible achieve high Q-factors in the order of 10^4 in UHV environment, thus NC-AFM is carried out in UHV conditions.

Part II.

Friction Anisotropy

3. Friction Anisotropy

The work presented in this chapter is based on the publication [3]. Friction forces arise at the interface of two bodies when they are in contact and sliding against each other. Most studies have focused on the friction vector in the direction opposite to the sliding direction, as this is the direction of friction generally expected but in some cases the friction vector may show deviation from being anitiparellel to the sliding direction and the magnitude of frictional force could depend on the direction of sliding. This is termed frictional anisotropy. Studying anisotropic behavior of friction gives an insight into the symmetry of the surfaces in contact. A direct consequence of the symmetry of the atomic surface structure is anisotropy of friction and wear, the latter of which can be observed on a macroscopic scale[22].

With the introduction of friction force microscopy, atomic-scale friction processes have become experimentally accessible [49]. The atomic force microscope (AFM) has become a powerful tool for mechanical property characterization, visualization, probing, and manipulation from micro scales down to nanoscale. Atomic force microscopy can provide spatial resolution of a few nanometers and below. The actual achievable resolution depends on the size of the AFM tip and the mechanical properties of the sample under study. In this work we have studied anisotropic behavior of friction on graphitic materials as these materials have gained importance as solid lubricants.

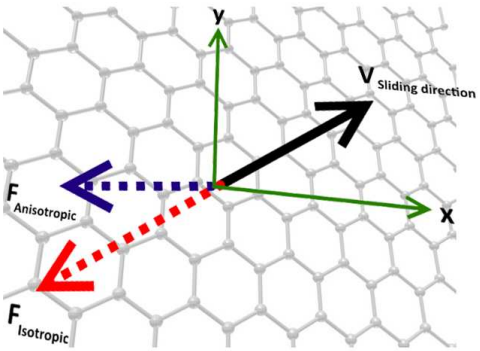

Figure 3.1.: Anisotropic friction scenario. In isotropic cases the friction vector (dotted red line) will be anitiparellel to the relative velocity vector (solid black). But in case of anisotropic friction, the friction vector (dotted violet) deviates from the antiparellel direction

3.1. Why graphene for tribology?

Reducing friction and wear is a long standing goal of science and technology. Apart from the intensive research that is focused on graphene for future electronic applications, there is much room for research on its tribological characteristics. As a lubricant graphene remains relatively unexplored. Graphene, apart from its well-established thermal, electrical, and mechanical properties offers unique friction and wear properties. Its high chemical inertness, extreme strength, and easy shear capabilities are the major attractive attributes for its tribological behavior. As a single or multilayer, it can be applied to nano-scale or micro-scale systems such as micro electromechanical systems (MEMS) and nano-electromechanical systems (NEMS) with rotating, and sliding contacts to reduce friction, and wear. Lee et al. [42] tested the mechanical properties of graphene and confirmed it to be one of the strongest materials ever measured. In this work, the authors used free-standing graphene membranes and analyzed them with a diamond atomic force microscopy (AFM) probe, which allowed measuring the breaking strength. The measured strength of a defect-free graphene sheet is in the order of 1 TPa. All the properties mentioned above make graphene very attractive for demanding tribological applications to achieve low friction and low wear regimes. Another important factor with effects

in reducing friction is commensurability between contacting surfaces. It has been accepted through experimental results that the frictional force strongly depends on the commensurability of contacting surfaces in the way that a commensurate contact usually leads to considerably larger friction than an incommensurate one. By controlling the lattice misfit angle between the two contacting lattices, the friction was found to reach its maximum in the commensurate case, but turned to a very low value close to measurement limitations for the incommensurate case, suggesting a state of superlubricity.

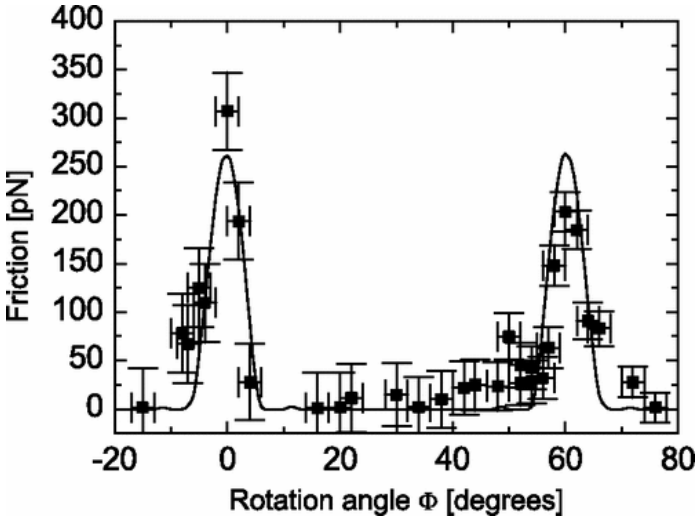

Figure 3.2.: Average friction force versus rotation angle of a graphite sample. Two peaks of high friction were observed having magnitudes of $300pN$, and $200pN$ at angles of 60°. [19]

Dienwebel et al,[19]studied friction between a graphene flake and a graphite surface as a function of relative orientation between two them. The experiment was carried in a wearless regime. The plot in Fig3.2 of friction versus relative sliding direction depicts the experimental results. Friction forces ranging from moderate to ultra low values were measured depending on the degree of commensurability between the lattices two surfaces. The ability to achieve such a state of ultra-low friction is termed super lubricity (a word coined by Hirano at al[31]).

3.2. Exploring anisotropy and previous works

The first measurement of transverse component of friction dates back to the work of Ernest Rabinowicz [63]. His work focused on the measurement of transverse component of friction when a hemispherical steel ball slides on a flat steel disc. A deviation of 3° between relative velocity vector and friction vector was statistically determined indicating anisotropy in friction force. Anisotropy in sliding friction has been observed for several surfaces by means of friction force microscopy and also in dynamic atomic force microscopy (AFM) experiments [79]. These studies include variations in friction upon rotating the sample [56]. The importance of the misfit angle in friction was first determined by Hirano et al [32]. Friction was found to increase when two mica sheets made commensurate contact.
Ultra Strong friction anisotropy is observed when the twofold surface of an atomically clean aluminum nickel cobalt quasicrystal slides against a thiolpassivated titanium nitride tip[57].

In an interesting study by Weymouth et. al,[79] the dependence of the scanning direction on measured lateral forces in noncontact mode of AFM was discussed. They have shown that the forces are measurably different, depending upon the scanning direction. Friction differences between scanning forward and backward along the same line arising due to the asymmetric molecular orientation are presented in [10][71]. A deviation of the direction of the friction vector from the pulling direction when scanning in different directions on a crystalline surface are discussed in the literatures by [34, 11, 12]. These observations of anisotropic fiction phenomena have been modeled by various approaches [12, 30, 73, 26, 77],. There are, many examples in the literature of direction locking, when particle motion does not following forced path, but rather the underlying symmetry [38, 72]. Without any external driving, directional dependence of diffusivity is also common on rectangular lattices or along step edges.

An interesting study by R. M. Overney et al [56] showed the effect of anisotropic frictional forces on a bilayer lipid film. In this study a deviation in frictional values

was found for different molecular alignment . Friction anisotropy arising due to the molecular orientation appeared as contrast difference in friction force images when a Silicon Nitride tip slid across the domain boundary of lipid layer . The inhomogeneity in friction on a laterally anisotropic and highly ordered organic monolayer showed that the contrast reflects the molecular arrangement. This kind of a local anisotropy of friction is shown to originate in different crystal orientations on the surface. A confirmation of this effect was reported in a paper by Takano and Fujihira [56]. An AFM tip was pulled along a molecular layer where the molecules were locally all tilted in the same direction. Liley et al. [44] observed a flower shaped molecular island on mica substrate (see Fig3.3) showing different domains distinguished by their frictional value. Interestingly, these domains and were not observed in topography.

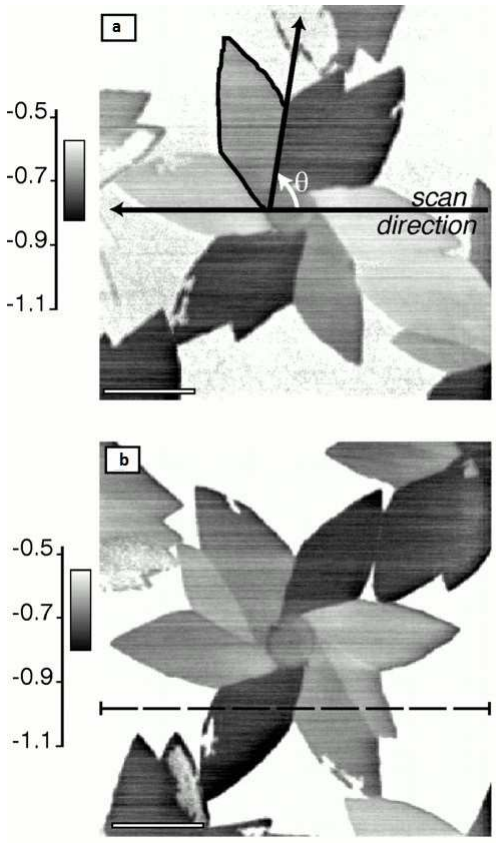

Figure 3.3.: (a) Flower shaped islands of thiolipid monolayer on mica. Different domains can be differentiated according to difference in their frictional values. (b) After counterclockwise rotation of the sample by 70°[44].

In lateral force mode (LFM), the cantilever is slid perpendicular to the long axis of

the cantilever and the lateral deflection of the cantilever corresponds to the friction which is tangential. Scanning along any arbitrary directions other than perpendicular to the long axis of the cantilever would make cantilever to buckle. Another aspect of scanning along different axis is the anisotropy of the cantilever itself. The spring constant of the cantilever is varying as a function of the angle. A detailed account of effects of cantilever anisotropy due to scanning direction on atomic stick slip phenomena and static friction is presented by Hosson and Kassermakers[35].

Recently, a new mode of scanning the sample in AFM was reported [34] . In this mode, ultrathin (1 to 2nm) organic films polycrystalline were imaged with striking contract. Different domains on the surface with dissimilar orientation differentiated by their frictional value. The scanning direction in this mode is always parallel to the cantilever long axis, thus this mode of operation is different from lateral force microscopy (LFM). Any twist in the cantilever resulted from shear forces at the tip which are transverse to the scanning direction. Friction anisotropy in this case is due to the orientation of crystalline grains on the surface.

In the past some of the studies focused the phenomena of preferred sliding direction [70, 17] and some other have focused on the tangential component of friction force [68] but no literature have connected these two. Theoretical studies of anisotropic effects in atomic scale when an ultra sharp AFM tip terminated with single atom slid on 2D systems, have been presented by E. Gneco et al[26]. In this paper theoretical accounts for anisotropy effects experienced by a point mass for different sliding directions on surfaces of different lattice symmetries like square and honeycomb lattices have been studied based on the Prandtl -Tomlinson model. The authors have shown that the anisotropy in the kinetic friction is high on square lattices compared to honeycomb lattices and considering a honeycomb lattice as a substrate, they show that the magnitude of kinetic friction on such surfaces like graphene has a periodicity of 60°.

3.3. Experimental design

In AFMs the lateral deflection of the cantilever is a result of the force applied to the tip when it moves horizontally across the sample surface, and the magnitude of this deflection is determined by the frictional force. Here it is assumed that the friction is always in opposite to the direction of sliding. If the friction force is anisotropic, then in addition to the twisting there will also buckling of cantilever involved FigFigure 3.4b on page 42. For the total friction force one need to measure both Cartesian components of the friction vector. In a work by Campione [11] , it has been shown that the hysteresis in the lateral deflection signal and the height signal from the piezo actuator (voltage fed to the piezo actuator in order to keep the normal force exerted by the cantilever on the surface constant) when scanning in constant force mode, can be mapped to the **x** and **y** component of actual friction force respectively. The reason for subtracting the signals from forward scan from backward (hysteresis) scan direction is to exclude material induced effects but topography induced effects remain unaltered [6]. According to this study for a cantilever sliding in any arbitrary direction, the photodiode signal due to twisting and buckling of the cantilever gives the **x** and **y** components of the friction force. In our studies we will refer to these force components causing twisting and buckling as **x**- forces and **y** forces respectively. In our friction measurements with an AFM we determine the Cartesian components of friction from the vertical signal and the torsional signal of a rectangular cantilever. For all our experiments we employed a soft contact mode cantilever (NANOSENSOR PPP-CONT), nominal stiffness 0. 2 N/m. Extra care was taken to mount the cantilever exactly perpendicular to the fast scanning direction at 0^0 scanning angle in the friction mode of the AFM. A small normal force (10–12 nN) was chosen to ensure wearless scanning of the surface, which was confirmed by subsequent imaging.

In our experiments, all scans were recorded at constant height mode, i. e, with the feedback control for the z position was switched off. In our case we map the hysteresis of vertical deflection signal to the **y** component of the friction force vector. The angle dependent friction measurements were performed for different scan sizes ranging

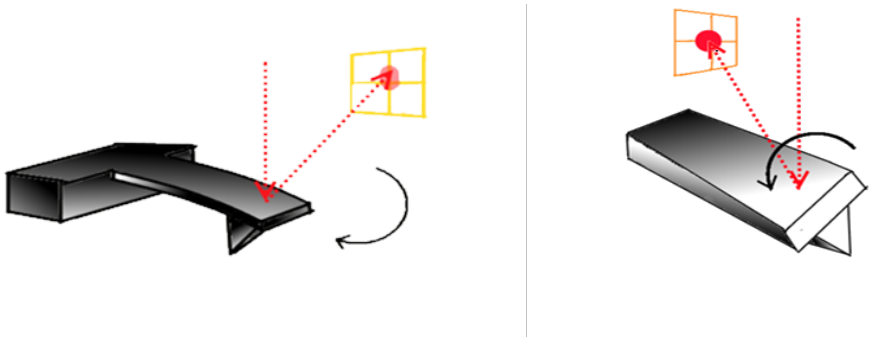

(a) Buckling of cantilever for scanning direction other than that of LFM configuration

(b) Twisting of cantilever

Figure 3.4.: Cartesian components of total friction force are extracted from twisting and buckling of cantilever during the scanning

from $(100nm)^2$ down to $(5nm)^2$. Scanning direction between successive frames was changed in steps of 10^0 or 5^0 starting from zero degrees to 360^0. Average values for frictional **x** and **y** forces were calculated by subtracting the average value of forward and backward signals in a cropped scan frame to exclude effects of directional change.

3.4. Scanning schemes

Scanning could be performed in two configurations. In the first one is keeping the scanning direction fixed and changing the orientation of the sample between successive scans. In another scheme the relative orientation of the sample and the cantilever is fixed and the scanning direction changed between successive frames. We adopted the second scanning scheme in our experiments in Fig3.5b.

3.4.1. Calibration

Since the rectangular cantilever has different stiffness along its short and long axis, a cantilever dependent calibration factor must be extracted and normalized in order compare and calculate the total friction for any direction of sliding. This was done by performing direction dependent friction measurement on an isotopic surface which in our case was a silicon oxide surface (an oxidized silicon wafer). Both the x and y components of friction must be of equal strengths for an isotropic surface [12].

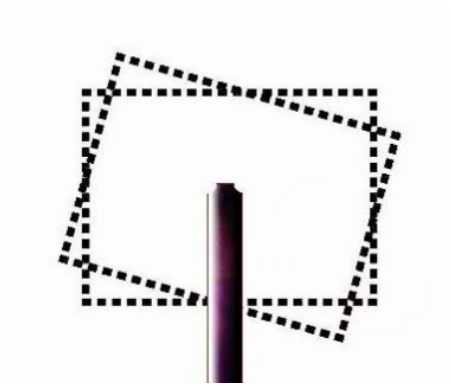

(a) Scanning along a fixed direction but the sample orientation is changed between successive imaging.

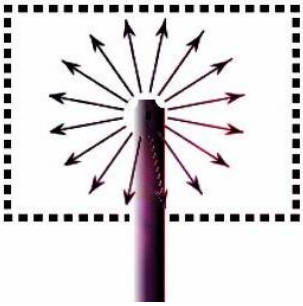

(b) Relative orientation between sample and the cantilever is fixed but the scanning direction is changed between successive imaging.

Figure 3.5.: Two possible scanning schemes. In all our experiments we follow the scheme3.5b

The forward-backward signal is measured for lateral and vertical deflection signals and plotted them against the scanning direction are fitted to simple sine and cosine functions. Then the ratio of the peak values from the fitted curve see Fig3.6a and Fig3.6b is used to normalize the measured x and y forces. The same cantilever is employed for the further experiments on HOPG and graphene.

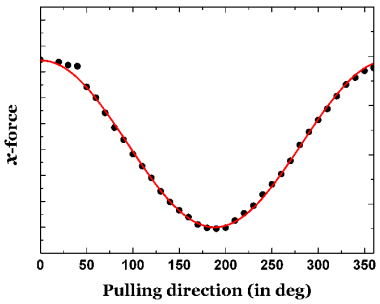

(a) LFM signal forward - backward plotted against pulling direction

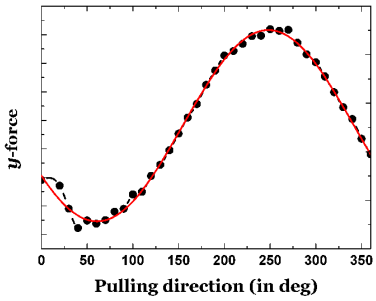

(b) Vertical deflection signal forward - backward plotted against pulling direction

Figure 3.6.: Cartesian components of friction vector for an isotropic SiO_2 surface plotted against the pulling direction. These curves can be best fitted with a sine function (Red curves show fitting function)

After normalizing the signals we plot the x and y components of friction on SiO_2 into a Cartesian force map of the friction force. The points on the map must trace a

circle with equidistant points indicating that the friction vector is always antiparallel to the sliding direction as observed in the plot below Fig3.7.

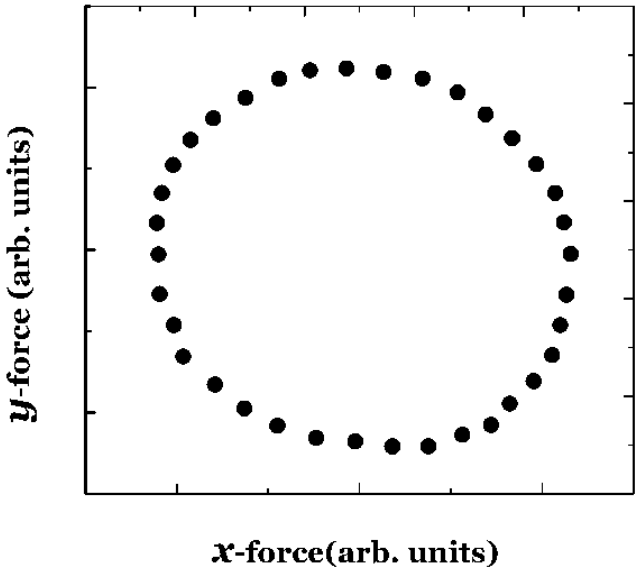

Figure 3.7.: Cartesian plot of friction forces on an isotropic sample SiO_2

3.4.2. Friction anisotropy on graphite

First friction anisotropy measurements are carried out on highly ordered pyrolytic graphite (HOPG) sample. Prior the the actual measurement several scans ranging from $3\mu m \times 3\mu m$ down to $5nm \times 5nm$ were performed on an atomically flat area until an image with regular atomic stick-slip see the Fig3.8 slip is obtained. The maximum scan area chosen for friction anisotropy experiments was $(100nm)^2$. After completing the experiment, the scan area is reduced to next desired desired scan size this is continued until a small scan area of $(5nm)^2$ is reached.

Matlab is used for the data analysis. The x and y forces for different scanning directions are obtained by subtracting cropped image data of backward from forward scan. For each scanning direction an image of 256 lines with 256 pixels is recorded. These images are cropped to exclude turning point effects. An average value of friction is extracted by averaging each line and again averaging across lines. Thus a single value for friction is obtained from each image for lateral and normal deflection.

The vector on a Cartesian plot gives both the direction and magnitude of friction vector.

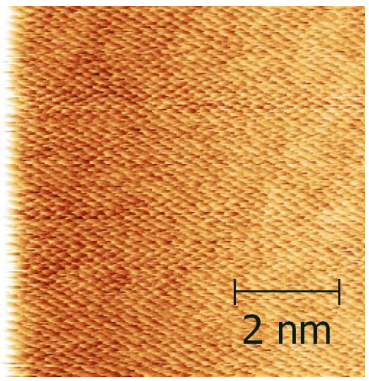

Figure 3.8.: Typical atomic stick slip image obtained on highly ordered pyrolytic graphite (HOPG) surface. Here the scan size is $(7nm)^2$. The stick slip periodicity matches the periodicity of the substrate lattice.

The Cartesian plot of friction force on an atomically flat area of highly oriented graphite is shown in Fig3.9a . In contrast to the Cartesian plot of friction on the SiO_2 surface, the plot for the graphite surface shows that the friction vectors are locked in six groups, where data points are clustered and which form a hexagonal pattern, indicating a strong friction anisotropy. By comparing the directions of friction vector groups with the orientation of the graphite surface which is known from the atomic stick-slip results, we find that the six zigzag directions are preferred sliding directions which will be explained in the next page.

The angular deviation between friction vector and pulling vector is plotted as a function of the pulling angle. the angular deviation is calculated as follows if the direction of pulling is θ_p, angular deviation is β ,and the Cartesian components of friction vector are $F_x$and F_y

$$\beta(deg) = \theta_p - \{180/\pi * [tan^{-1}(\frac{F_x}{F_y})]\} \tag{3.1}$$

In the plot of the angular deviation between sliding and total friction vectors, see Fig3.9b there is a jump at each preferred sliding direction by on average 28.5°. These jumps speaks for the strong tendency of the surface to force the contact into

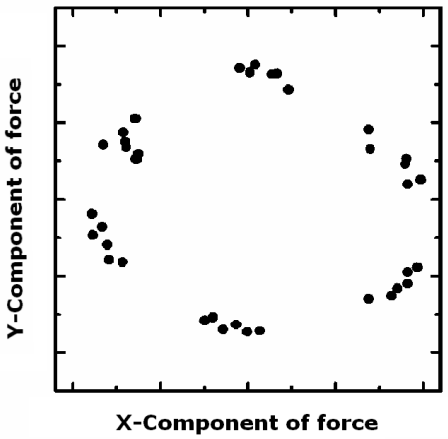

(a) Normalized friction vectors measured for pulling directions between 0°and 360°in steps of 10°on an atomically flat surface area of graphite. The scan size 27 nm x 27 nm

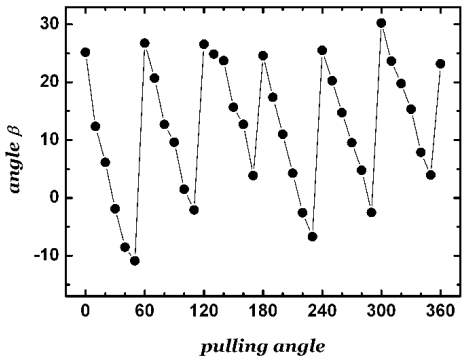

(b) Angle between pulling direction and the friction vector

the preferred sliding directions, which changes abruptly the sign when crossing the preferred sliding direction.

The results in Fig3.9 demonstrate that the friction anisotropy due to preferred sliding directions is also found on epitaxial graphene layers grown on a SiC(0001) surface. The surface orientation was different by about 30° compared to the graphite sample are shown in Fig3.9a. Similar to the results in Fig3.9a, the friction vectors form six clusters in a hexagonal pattern. But two friction data points corresponding to sliding directions 70° and 310° lie in the middle between two groups. For these two directions, the pulling direction has met almost exactly one of the preferred sliding directions, so that the friction vector is directed opposite to that of sliding direction see Fig 3.10.

In order to understand the experimental results of anisotropic friction on six fold symmetric surface, consider the scenario depicted in Fig3.11a. Solid arrows indicate the pulling direction, dashed arrows the corresponding direction of the friction force vector. We have six preferred directions on graphite surface. Consider the case when the pulling direction is not along one of the preferred directions, Unlike for the isotropic case, the friction vector here will have an additional component towards one of the preferred sliding directions which forces the tip to move along the preferred

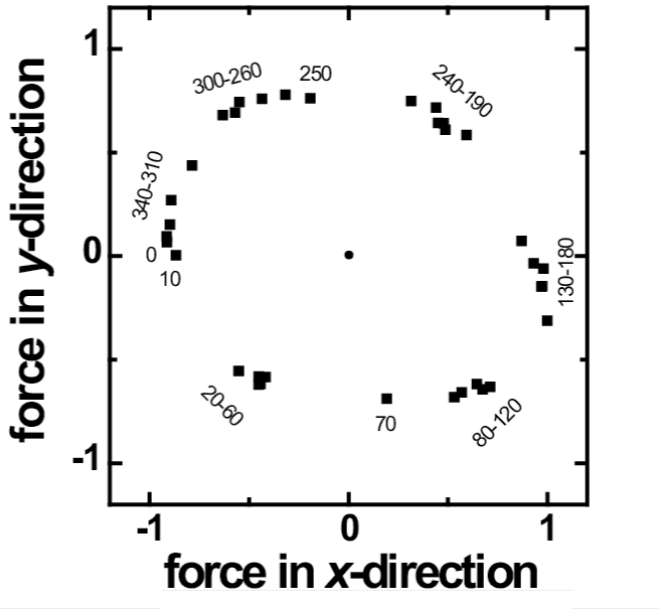

Figure 3.9.: Normalized friction vectors measured for pulling directions between 0°and 360° in steps of 10° on an atomically flat surface area of graphene. The scan size 30 nm x 30 nm. Data point are named corresponding to their pulling direction. Two data points for 70° and 310° lie out side from two clusters. For these two directions, the pulling direction has met almost exactly one of the preferred sliding directions hence the friction vector points exactly opposite to the direction of sliding.

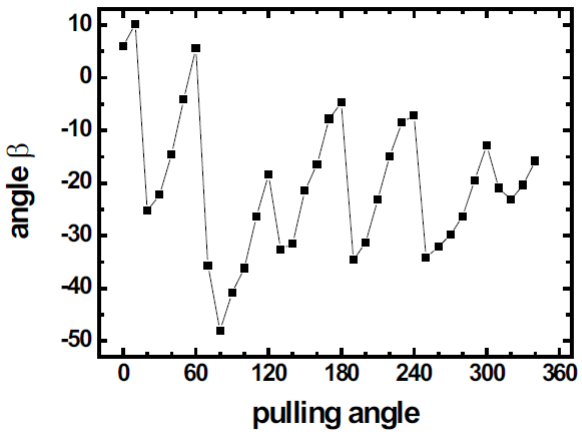

Figure 3.10.: Angular difference between the pulling direction and the friction vector for the graphene surface.

direction.

The angular deviation in friction with the sliding direction is maximum for pulling directions which are very close to the preferred direction and which is manifested as anomalous stick slip pattern in friction force images (Fig3.14). In our experimental results, a strong component of the friction force component towards the zigzag directions is found for all pulling directions close to the zigzag directions, therefore the zigzag directions are preferred sliding directions.

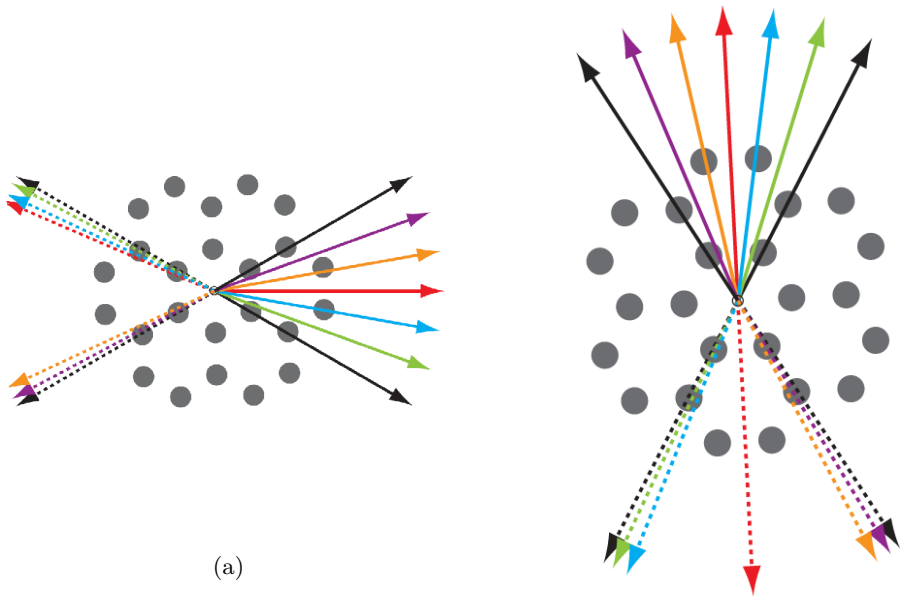

(a) (b)

Figure 3.11.: Schematic experimental scenario on graphene and Schematic representation anisotropic friction process on sixfold symmetric surfaces

The anisotropic scenario on graphene is schematically represented in Fig3.11b , where the centered red arrows correspond to the pulling direction of 70°. The plot of the angles between pulling and friction directions in Fig3.10 is less regular than the one in Fig 3.9b, but still shows the characteristic jumps at the six preferred sliding directions. The corresponding lateral force traces in Fig3.12 and the lateral force images Fig3.14 for different sliding directions around preferred directions, makes it easy to visualize the effects of anisotropy. In Fig3.12 each trace reports the x-force over the scan length of 30 nm for the different pulling directions. We have

already determined that the pulling angles of 70° correspond to sliding along a preferred direction, therefore we observe almost no force fluctuation for the 70° pulling direction which in this experiment lies almost parallel to the long axis of the cantilever. In contrast, there is a pronounced saw tooth signal for the neighboring sliding directions i,e 60° and 80°, with a characteristic length of 1 to 1. 5 nm. The distance between adjacent atomic rows of graphene is $\sqrt{3}/2 \times 0.246nm = 0.213nm$, and a misalignment of 10° in sliding direction from from preferred direction should in principle produce slip events every $0.213nm/tan10^{\circ} = 1.21nm$. This is in good agreement with the experimental observations. But for the opposite pulling direction 250°, the zigzag direction is not perfectly matched, therefore slip events occur at every 5nm when the tip crosses every adjacent row. From the periodicity of slip events, we calculated the misalignment in case of 250° sliding to be 2.4°. Our interpretation of the sawtooth signal is depicted in Fig3.13.

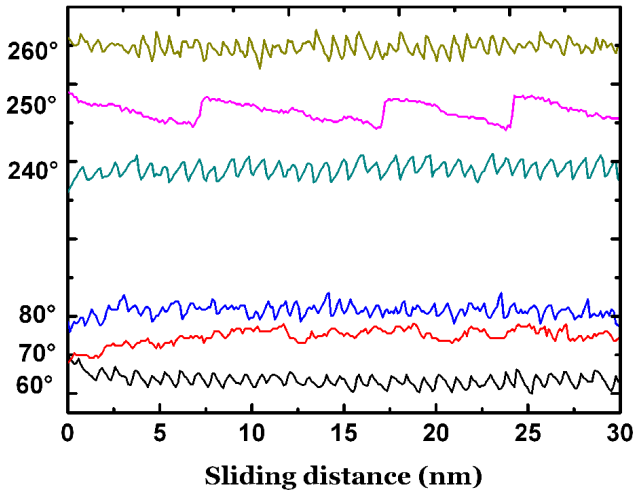

Figure 3.12.: Traces of the force in x direction for pulling directions close to a preferred sliding direction. Since in this configuration the preferred sliding direction is almost parallel to the long axis of the cantilever, forces perpendicular to the pulling direction are measured with high sensitivity as x forces.

Friction force images for different sliding directions on graphene are shown in Fig3.14. For a sliding angle of 250° (Fig3.14b) we have observed maximum anisotropy,

since this direction of sliding is slightly off from one of the preferred sliding directions, Fig3.14a and Fig3.14c present the friction images for the direction of sliding $\pm 10°$ around 250^0. Here the degree of friction anisotropy is comparatively less. As the angular difference between the forced scanning path and one of the preferential sliding directions increases, the tip traverses across more number of atomic rows and hence the transverse force that builds up in the cantilever between two slip event is less (refer to Fig3.13). There exists a minimal distance,which tip has to travel in order to store adequate restoring force which in turn causes a first slip motion. This explains the lesser degree of anisotropy for small scan sizes, which is in agreement with the experimental observations.

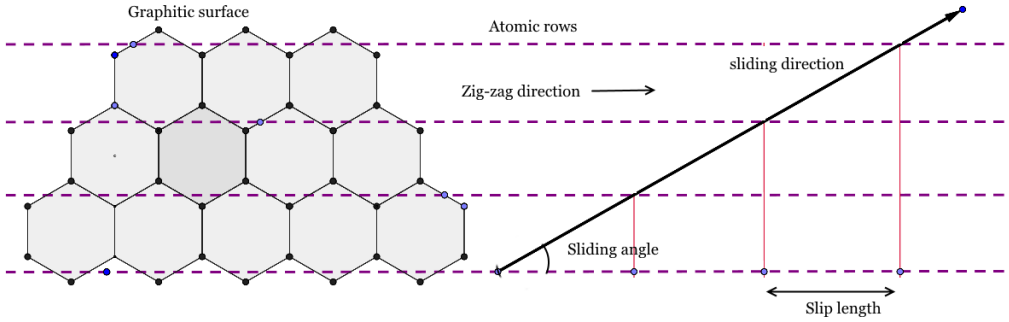

Figure 3.13.: Explanation for the observed anomalous stick slip behavior when the pulling direction deviates slightly from one of the preferred sliding directions. .

To check the validity of scan size effects on the anisotropic behavior, we performed similar measurements on graphene at a larger scan area of $(100nm)^2$ (refer to the Fig3.15). Here the scanning angle $20°, 80°, 140°$, and $200°$ are the directions which only slightly deviate from one of the preferred sliding directions, therefore we observe an extended stick slip periodicity which is caused by the tip hopping from one atomic row to another after traveling in one preferred direction for longer durations. Since the scan size is larger and the deviation from preferred direction is smaller in case of $20°, 80°, 140°$, and $200°$ directions , the tip will spend more time along nearest preferred directions before jumping to the next one. During this time tip acquires enough restoring force. Only when a certain threshold is reached the tip makes a

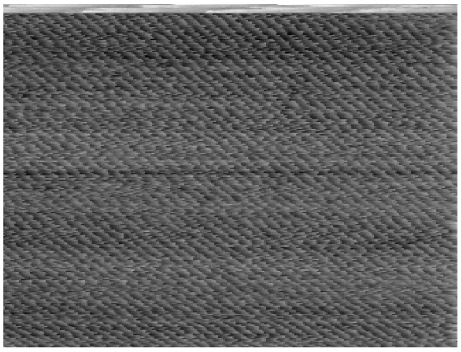

(a) sliding direction 240°

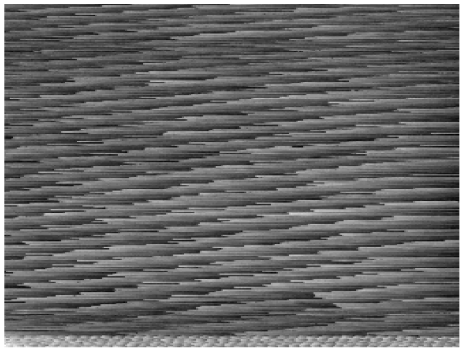

(b) sliding direction 250°

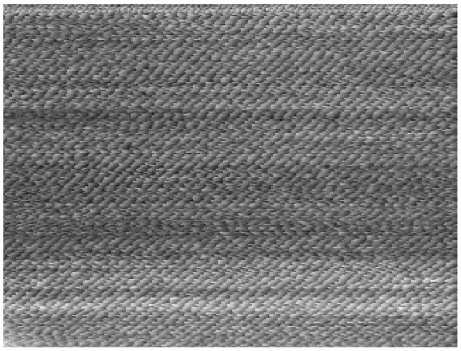

(c) sliding direction 260°

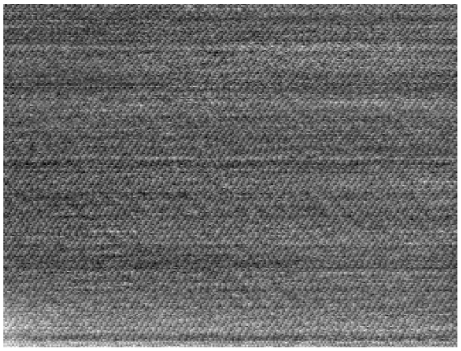

(d) sliding direction 270°

Figure 3.14.: Friction image for different sliding directions 230°,240°,250° and 260° showing anomalous stick slip periodicity which are due to the strong transverse component of friction force. Scan size is $(27nm)^2$ Highest stick slip periodicity found for the sliding direction 250° in Fig3.14b which is slightly off from on of the preferred directions. For other directions around this one we observe a lesser degree of anisotropy

huge jump to the next preferred direction. This is manifested as extended slips in the friction images.

3.5. Simulation methods

Our experimental results are also supported by simulations carried out by Astrid de Wijn. Sliding friction on graphitic surfaces has been modeled in [73, 26, 77, 70]. Here this simulation is based on the Prandtl-Tomlinson model [74, 61, 62]. This model is used to explain atomic stick slip process in friction experiments and many other phenomena. Basically in this model, a rigid support which is coupled to a

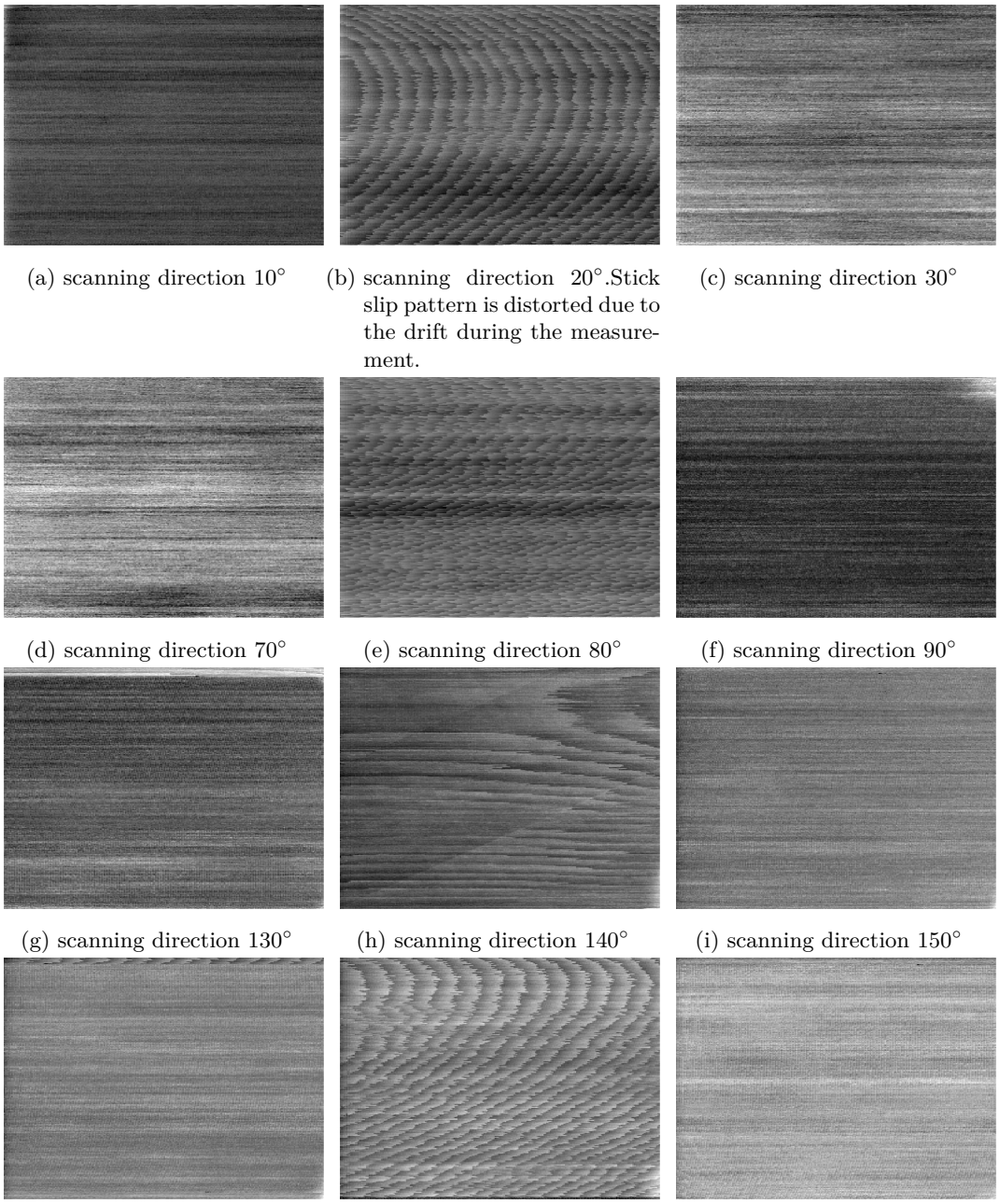

(a) scanning direction 10°

(b) scanning direction 20°.Stick slip pattern is distorted due to the drift during the measurement.

(c) scanning direction 30°

(d) scanning direction 70°

(e) scanning direction 80°

(f) scanning direction 90°

(g) scanning direction 130°

(h) scanning direction 140°

(i) scanning direction 150°

(j) scanning direction 190°

(k) scanning direction 200°.Stick slip pattern is distorted due to the drift during the measurement.

(l) scanning direction 210°

Figure 3.15.: The degree of friction anisotropy is found to increase with scanning size. Friction images for scanning size $(100nm)^2$ are depicted here. Different sliding directions showing anomalous stick-slip pattern repeating after every 60° of sliding angle. Maximum stick slip periodicity is found for the sliding directions $20°, 80°, 140°$ and 200°, which are slightly off from one of the preferred directions.

harmonic spring terminated with a tip moves in a constant velocity and the tip is subjected to a substrate potential. The tension in the spring equals the force needed to keep the support moving in the same directions and at constant velocity

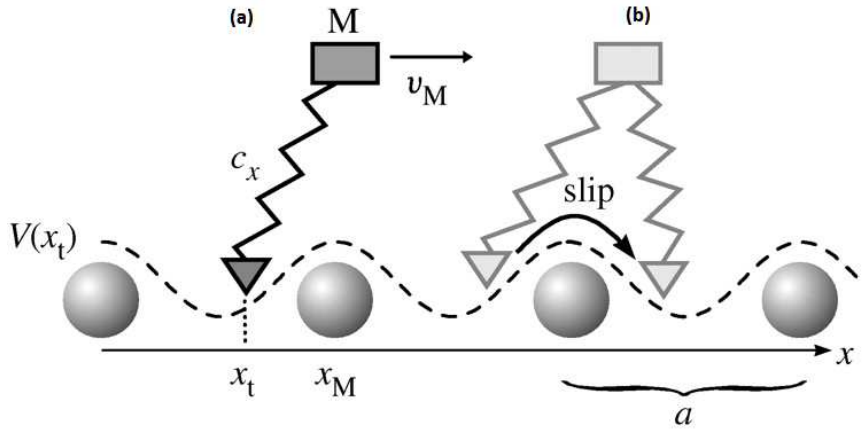

Figure 3.16.: (a) A schematic diagram showing a tip sliding on an atomically flat surface based on the Prandtl–Tomlinson model. An atomically sharp tip is coupled elastically to the body M by a spring with spring constant c_x in x- direction. x_t represents its position within an external potential V(x_t) with lattice periodicity is a. If x_t=x_M, the spring is in its equilibrium position. For sliding, the body M is moved with a velocity v_M in $x$direction. (b) A schematic view of the tip movement in a sinusoidal potential. (Image source: [33])

The basic parameter used in our simulation is as follows. The substrate is a regular arrangement of carbon atoms and the tip is a hexagonal graphite flake of 216 carbon atoms. Both the substrate and graphite flake are rigid. The spring constant of modeled cantilever was 1N/m. The normal load parameter was set to $108nN$ and the orientation of the flake relative to the substrate was commensurate. The sliding speed was $v = 2m/s$. Typical velocities used in experiments are much lower than this value. But these parameters were sufficient for the system to exhibit stick-slip bheviour as observed in the experiments.

3.6. Comparison with the simulation results

Friction anisotropy on epitaxial graphene on SiC(0001) for a smaller scan range and a finer resolution in pulling angles is reported in Fig3.17a. The overall shape of the Cartesian friction plot is similar to the results for larger frames Fig3.9a and and is very well comparable with the simulation result in Fig 3.17b. We don't see clearly separated clusters of points, but the relative density of data points at the corners is higher compared to other parts of the curve. The absolute friction values are higher in armchair directions as compared to zigzag directions. The deviation of the absolute value of the friction force between initial and final state could be due to a gradual change in the tip-sample contact area over the course of the longer duration of the experiment. At small scan sizes, and small angular deviations from preferred direction, the tip traverse across fewer atomic rows (refer to the Fig3.13) hence a smaller restoring force builds up to cause initial lateral jumps will be weak.

Lateral force traces of the experiments in Fig3.17c are successfully reproduced in the simulations. The plot in Fig3.17d shows the x and y component of friction force for three sliding directions. As it can be readily seen the degree of anisotropy is high when the sliding direction is 1°. Upon changing the sliding direction to 6°, the tip crosses a higher number of atomic rows and the sticking duration becomes shorter. This behavior continues and the friction decreases even more when was sliding direction was 11°. A similar behavior was reported for graphitic surfaces [64] and was attributed to puckering of the top most layer. Since our the simulations the substrate was a rigid surface, it is improbable that the puckering is the reason for the extend stick-slip behavior.

3.7. Discussion

Our experimental results show a strong anisotropy of single-asperity friction on graphitic surfaces. Since graphene is an attractive material as a lubricant, we have studied the anisotropic behavior of friction when an ultra sharp silicon cantilever

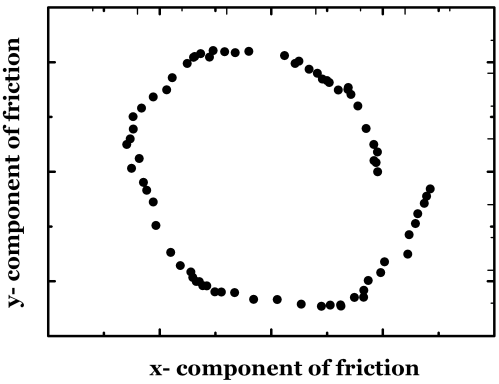

(a) Cartesian plot of friction vectors measured for pulling directions between $0^{\text{Å}^\circ}$and $360^{\text{Å}^\circ}$ on an atomically flat surface area of graphene. The scan size 5 nm x 5 nm and a finer angle resolution of 5°

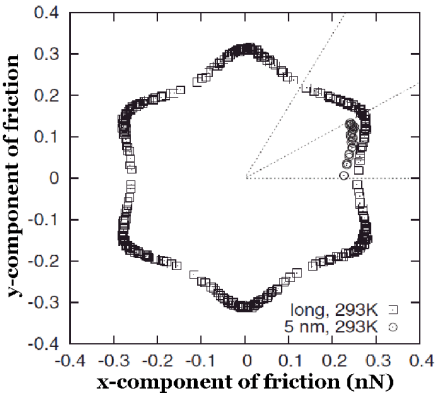

(b) Friction anisotropy result from the simulation: Cartesian plot of friction vector for a tip of a 216-atom graphite flake sliding on graphitic surface at room temperature with an angular resolution of $1\circ$. Scan size being $(1nm)^2$

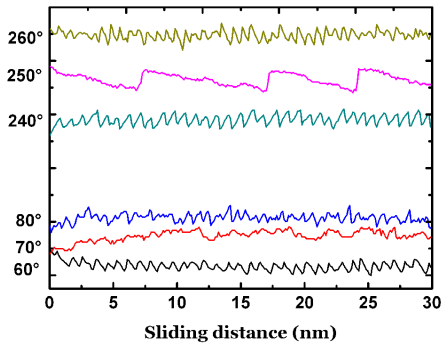

(c) Result from the experiment lateral signal exhibiting extended stick slip behaviour when the sliding directionis 250° which is slightly off from on of the preferred directions. As soon as the sliding direction changed by ±10° both the slip periodicity and the amplitude diminishes.

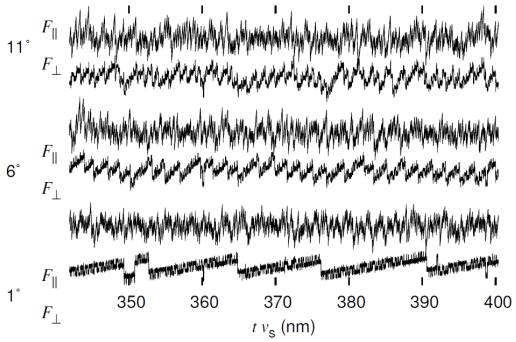

(d) Simulation result: Lateral force traces for a tip sliding around one of the preferred directions matches exactly with the experimental results.

Figure 3.17.: Correspondence between the experimental and simulation results

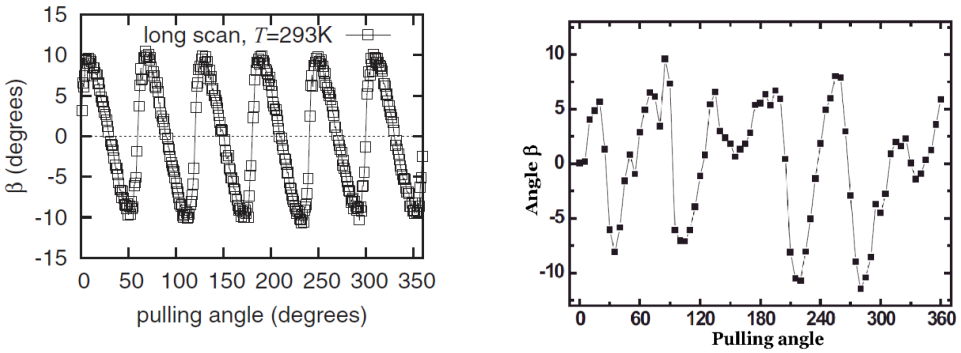

(a) 5°Deviation between friction and relative velocity vector is observed in simulations for pulling directions from zero to 30°.

(b) Angle between pulling and friction directions as a function of the pulling angle. The scan size $(5nm)^2$ and a finer angular resolution of

Figure 3.18.: Comparision between Angle between pulling and friction vectors between experient and simulation fo small scan size. Scan size in the experiment $(5nm)^2$ and $(1nm)^2$ in simulation.

is slid on different directions. Interestingly we have noticed that the friction is antiparallel to pulling only when sliding along zig-zag or armchair directions. Zig-zag directions are preferred sliding directions. When the forced path of the AFM tip is slightly off from one of this zigzag directions, the tip experiences a strong transverse force which tries to bring the tip into one of nearest zigzag atomic rows. This is manifested as elongated stick slip pattern in the lateral force images. As a result, this angle between sliding direction and resulting friction vector jumps by up to a maximum of 30° from isotropic friction direction. Since the sliding path is directed by the piezo of an AFM, any deviation from the preferred sliding direction results in building torque in the cantilever due to the transverse friction force which pulls the tip towards one of the nearest zig-zag directions. When the restoring force in the cantilever becomes sufficiently larger than this transverse component of friction force, then the tip makes an abrupt jump to the next zigzag row. This is seen as elongated slip event in the lateral signal.

First we carried out our experiments on a HOPG sample surface, then we performed the same experiment on graphene layers grown epitaxially on SiC(0001), both show similar results indicating a strong anisotropy on graphitic surfaces. The degree

of anisotropy as expressed in the jump of the angle between pulling and friction decreases for very small scan sizes. The transverse component of friction vanished only when sliding along zigzag directions or along one of the armchair directions. Therefore, the Cartesian vector plots of friction force shows, clusters of points around arm chair directions. Experiments with higher angular resolution and smaller scan ranges reveal that the absolute value of the friction vectors is maximum in armchair directions and minimal in the preferred zigzag directions. Experiments also indicate that the degree of anisotropy is directly dependent on the sliding distance.

Since the contact area and the load are subjected to a sudden changes, this imposes some limitations on the possible duration of experiments and is hard to know the structure of the sliding tip before and after such changes. Simulation results for a sharp and a large amorphous tip show similar anisotropic behavior. Therefore the anisotropic behavior is independent of tip shape and geometry. A highly asymmetric tip, or a tip with different rotational symmetry than the substrate, may display some additional anisotropic effects, but anisotropy arising from the substrate lattice always exist. In all experiments, we have observed atomic-scale stick-slip with the expected hexagonal periodicity of graphene, which indicates that the tip is either amorphous silicon oxide or a graphene flake attached to it. If there was a graphene flake on the tip, then it is not rotated along the registry of the substrate [23]. Simulation results based on the Prandtl-Tomlinson model supports the experimental results. Experiment results are very well reproduced by simulations. The most important observation is that, when the sliding direction deviates slightly from one of the preferred directions then we see the strongest deviation in the direction of the friction vector.

Part III.

Friction studies on graphene

4. Ultra high vacuum system

4.1. UHV chamber design

UHV conditions for surface science experiments are necessary for two main reasons 1) to avoid scattering of electrons with gas molecules and 2) to provide an environment where an atomically clean surface stays clean during the course of experiment. UHV conditions are generally regarded as being in the region below 10^{-9} mbar.

The value of mean free path of molecules is gives an idea why the UHV environment keeps the surface cleaned for longer durations. The mean free path λ of molecules is

$$\lambda = \frac{k_B T}{\sqrt{2}\pi\xi^2 P}$$

where k_B is Boltzmann constant, ξ the molecular diameter, P is the pressure of the gas, and T is the temperature. It can be readily seen that the mean free path is very large in the order of 10^3 m at such low pressures. It means, the probability of two molecules striking each other is very low rather they stick to the walls of the chamber.

In surface science experiments involving ultra clean surfaces it is expected that the surface should stay clean during the length of measurement. So it is important to keep surface clean for longer durations. But the cleanliness of the surface is mainly dependent on how many molecules or atoms strike the surface from gas phase. In other words the incident flux of gas molecules should be very small to keep samples clean for longer time. For given pressure (P) temperature (T) the flux

of gas molecules hitting the surface can be calculated by combining ideas of statistical physics and the Maxwell-Boltzmann gas velocity distribution. The incident flux, f , is related to the gas density above the surface as

$$f = \frac{1}{4} \times n\tilde{c} \tag{4.1}$$

Where n is molecular gas density (molecules per volume) and $\tilde{c}$ is the avrage molecular speed

From the ideal gas law, number of molecules in given pressure and temperature is

$$n = N/V = P/(k_B T) \tag{4.2}$$

From the Maxwell-Boltzmann distribution of gas velocities we have the expression for $\tilde{c}$ as

$$\tilde{c} = \sqrt{\frac{8kT}{m\pi}} \tag{4.3}$$

By substituting equation (4.3) and equation (4.2) into equation (4.1)we get Hertz-Knudsen formula for the incident flux for the flux f as

$$f = \frac{P}{\sqrt{2\pi mkT}} \tag{4.4}$$

It can be readily observed that the molecular flux is directly proportional to the pressure inside the vacuum chamber.

Other important factor determining the time duration through which sample stays clean is the sticking coefficient, θ . This is the ratio between flux versus the number of molecules that adsorb to the surface. The sticking coefficient can have values in the range of 1 to 0, where a coefficient of 1 indicates complete adsorption, and zero is for no adsorption. The sticking coefficient can be a function of several variables like temperature, surface coverage, crystal face etc. By taking the sticking coefficient

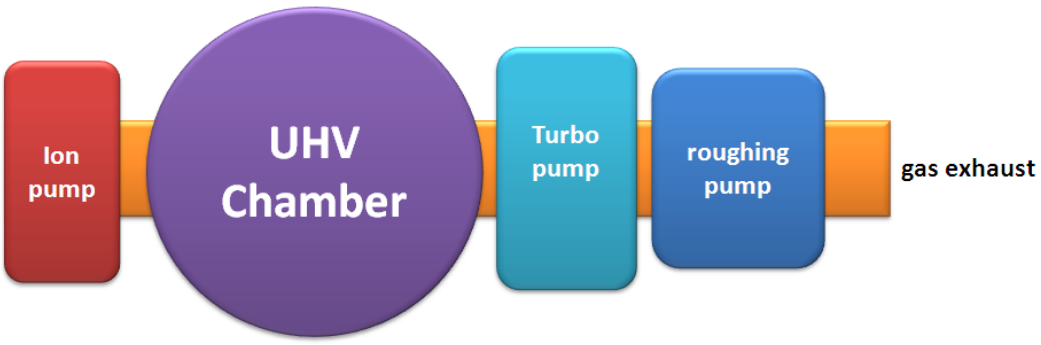

Figure 4.1.: Schematic diagram of UHV chamber and connected pumps showing the stages of pumping in order to achieve High vacuum.

as 1, a lower bound of time for monolayer contamination can be estimated for the pressure $10^{-10}mbar$ to be about 10^4seconds which is in the order of hours.

The flow of molecules under ambient conditions is called viscous and the flow under UHV conditions is called molecular. There is no single vacuum pump which works all the way from atmospheric pressure to ultra-high vacuum. Therefore, a combination of different pumps is necessary to achieve UHV conditions. A schematic diagram of a UHV chamber and different pumps is shown in the figure 4.1. Pumps commonly used to achieve UHV include: turbo-molecular pumps ion pumps, titanium sublimation pumps, and roughing vacuum pumps. Roughing vacuum pumps are concerned with the removal of the bulk gas from the system and they operate in the pressure region of $10^{-2}mbar$.

In addition to different pumps, an additional procedure called “baking” is required in order to achieve UHV. In the process of establishing UHV, the chamber is pumped down to a pressure of $10^{-2}mbar$ first with the help of a roughing pump. Further the chamber is pumped down to about 10^{-6} mbar pressure using a turbo-molecular pump. After reaching a pressure of 10^{-6} mbar, the baking procedure is carried out by enclosing the whole chamber with heat resistant boards. The chamber is heated (baked) to a temperature of about 150° C and maintained at this temperature for at least 48 hours. This baking procedure removes those atoms sticking to the walls of the chamber. After baking, the heat shields are removed, and the chamber is

allowed to cool down. When the chamber reaches room temperature the pressure in the chamber should be in the UHV region. In addition to the turbo pump, the UHV chamber is also equipped with an ion getter pump and a titanium sublimation pump. These two types of pumps work only at low pressure and do not contain any moving mechanical parts, hence they do not produce any mechanical vibrations.

Basic element of an ion getter pump is a Penning trap. Penning traps use a strong homogeneous axial magnetic field (strength is around 0.12T) to confine a rotating cloud of electron near the anode. Any incoming gas will be ionized by these swirling electrons and the resulting swirling positive ions are accelerated towards a chemically active cathode. Since the cathode uses a chemically reactive titanium, two things can happen. Highly accelerated positive ions end up at the cathode by creating crates on the surface or they can remove titanium from the cathode material and sputter it onto the walls of the pump.

The operation principle of titanium sublimation pumps is fairly simple. They consist of three titanium filaments we can switch among these three since only one filament works at a time. A high current around 40 Amps is passed periodically through the titanium filament. Due to this high current, the filament reaches the sublimation temperature of titanium. Titanium evaporates and and the chamber walls become coated with a thin film titanium. Since clean titanium is very reactive, any residual gas molecules in the chamber which hits the chamber wall are likely to react and to form a stable, solid compound. Thus the pressure in the chamber is reduced.

4.2. Low-energy electron diffraction (LEED)

Low-energy electron diffraction (LEED) is one of the principal techniques for the determination of the surface structure of crystalline materials by bombarding with low energy electrons of typically in the range 20eV to 200 eV. and observation of diffracted electrons as spots on a fluorescent screen [76]. The LEED experiment exploits the wave nature of electrons with well-defined low energy . Electron waves

incident normally on the sample with a well-ordered surface structure or a crystal surface with an adlayer. In order to visualize the electron diffraction pattern, the back scattered electrons are made to hit a fluorescence screen. A schematic experimental set-up is shown below in figure 4.2.

An electron gun accelerates electrons toward the sample surface. The filament of the electron gun is held at a negative potential V_{FIL} so that electrons acquire a kinetic energy eV_{FIL} .The energy of the incident electron beam is directly related to de Broglie wavelength of the beam as

$$\lambda = \frac{h}{\sqrt{2mE}}$$

where E is is in eV, m is the mass of electron, and h is Planck's constant. The kinetic energy of the electron beam can be adjusted by adjusting the potential of the filament. The LEED optics consists a series of hemispherical grids stacked together with a phosphor coated fluorescence screen at the end, as shown in figure 4.2. In the LEED measurements, the accelerated electrons hit the sample surface and reflect backwards towards the screen. Normally, the first grid is towards the sample is held at ground potential. The second and third grids are held at a potential similar to the potential of the filament. These grids filter out inelastically scattered electrons from reaching the phosphor screen. The screen is held at a potential between 3 kV and 6 kV so that the energy of diffracted electrons can excite transitions in the phosphor to emit visible light. Since electrons behave as waves, their interference image on the screen represents the reciprocal lattice of the crystal. The diffraction pattern and the spot positions provides information on the crystal symmetry and rotational alignment of the adlayer (if present) with respect to the substrate. The lattice constant of the crystal can be deduced from measuring the positions of the spots on the screen relative to the center of the screen for a particular energy of electron beam.

Our UHV chamber is a MULTIPROBE system, from Omicron Nanotechnology GmbH. This vacuum system has two separate chambers: one for sample preparation

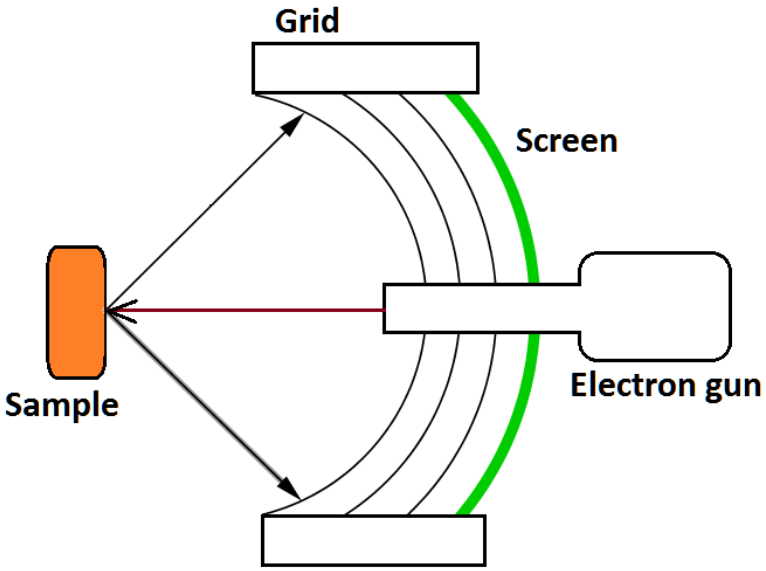

Figure 4.2.: LEED experimental set up

and another called analysis chamber houses an atomic force microscope . Both the analysis and preparation chambers are maintained at a pressure of 10^{-10} mbar. In the preparation chamber samples as well as cantilevers can be cleaned through Ar^{+} sputtering and heating. Heating of samples is possible at temperatures above 1000°. This chamber is also facilitated with a gas inlet for Ethylene and Argon, for CVD synthesis of thin films like graphene. Each chamber is separately connected to pumping systems, consisting of mechanical roughing, turbo molecular, ion getter, and titanium sublimation pumps. Both the analysis and the preparation chamber are equipped with transfer arms to move samples and cantilevers between the chambers. Cantilevers and samples can be brought to the AFM and positioned in-situ with a wobble stick. Samples and cantilevers are introduced via a load lock,which is pumped by the roughing/turbo-molecular pumps attached to the preparation chamber. The analysis chamber is equipped with a low energy electron diffraction (LEED) facility.

4.3. Instrumentation VT-AFM

Our UHV system houses a variable temperature (VT) AFM which is capable of probing the surface dimensions down to few nanometers with atomic resolution. A

complete UHV system , AFM and its components are shown in below figure 4.4.The VT-AFM provides temperature range for experiments by employing an integrated heating facility at the sample plate and the removable cooling connections. The achievable temperature range is from 25 K to 1500 K. The complete AFM set up is suspended by four springs, which avoid mechanical disturbances reaching to the AFM and they can be individually adjusted for leveling of the stage. In addition to that AFM also has a eddy current vibration isolation system which is to damp mechanical vibrations. This is a tip scanning microscope, where the laser optics and the probe are mounted on piezo actuator while the sample under study stays stationary. In this configuration it is easier to equip the system with temperature-control but it has higher noise level. In contact mode of operation, when the tip is not in contact with the surface, then one would expect no lateral deflection signal at the photo sensitive diode, but in this tip scanning configuration, even without the contact, raster movement of the piezo gives some signal at the photo diode. The piezo scanners in this tip scanning configuration move the probe in a curved path over the surface as shown in Fig.4.3, this curved motion results in a non zero voltage output at the photo diode and also "Bow or curvature" in the AFM images[58]. In such cases suitable polynomial must be subtracted from data in order to flatten the image.

The AFM cantilever dynamics is detected using the beam deflection scheme. A schematic diagram of the beam deflection scheme of this AFM is shown in figure 4.5.

A laser source is situated outside the vacuum chamber and the laser beam is directed to the cantilever through an optical fiber and mirrors. This AFM lacks lateral adjustment of laser beam on the photo diode i.e, the laser spot can only be adjusted in the y-direction. In situations where an atomic resolution imaging in contact mode is necessary, we employ an additional amplifier for the lateral deflection signal. The single tube piezo scanner has a scan range of $X : 4\mu m \times Y : 4\mu m$. Since the mirror motors are housed inside the vacuum chamber, they are remotely controlled. The AFM can operate in several modes which include Scanning Tunneling Mode (STM),

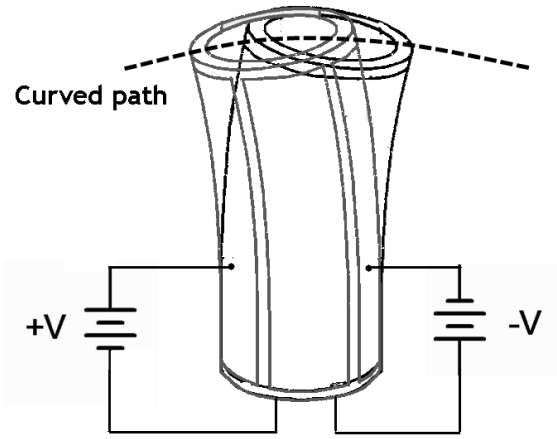

Figure 4.3.: Non linearity in the tip scanning configuration. The tip follows a curved path during the raster scan.

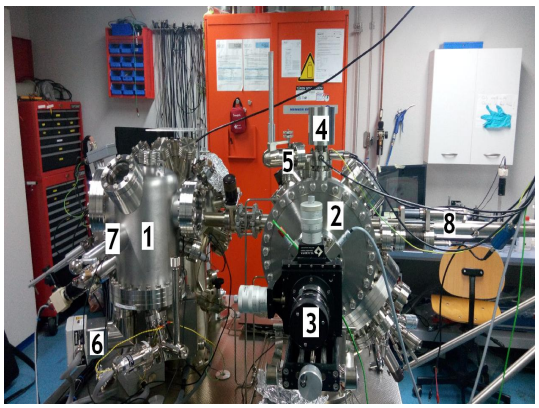

(a) Complete UHV system: (1) Analysis chamber, (2) Preparation chamber , (3) and (8) Transfer arms, (4) Sputtering system, (5) Gas inlet, (6) Laser source, (7) Wobble stick.

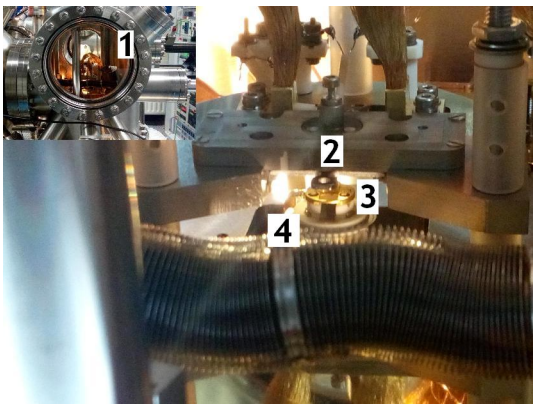

(b) A closer view of the AFM: (1) AFM inside the analysis chamber , (2) Sample holder plate, (3) Cantilever (4) Piezo actuator beneath.

Figure 4.4.: (a) UHV system and labeled components, (b) Atomic force microscope inside the analysis chamber

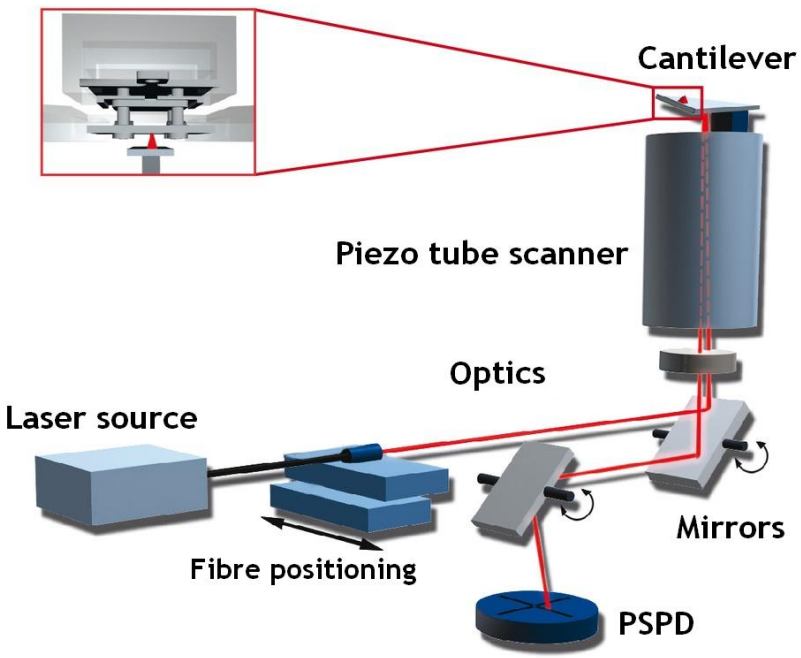

Figure 4.5.: Beam deflection scheme employed in our UHV-AFM system (image source: www.omicron.de)

contact mode and non-contact modes (nc-AFM, Kelvin probe force microscopy, EFM, MFM). As control electronics for this AFM we used a Nanonis's SPM control system.

5. CVD synthesis of graphene/Pt(111) in UHV

5.1. Literature review

The discovery of graphene[55] has propelled research on graphene hoping to open up new possibilities of using graphene for the future technology. Many studies have focused on growing graphene on metal substrates like Pt, Ir [14, 15] and Cu. Unlike other transition metals graphene shows very weak interaction with platinum surface, this makes it very interesting to study mechanical and electric properties of graphene/platinum system. There is literature from the mid 60's reporting the formation of graphite on metal surfaces like Pt and Ru when hydrocarbons dissociate on the metal surfaces [29, 27, 40]. These publications discuss the formation of graphitic overlayers on metals. In these early works graphene formation was monitored by Auger electron spectroscopy and low energy electron diffraction (LEED). Usually the Chemical vapor deposition method is preferred for growing graphene on metal substrates. Growth dynamics of graphene/metals systems for different metals have been summarized in a review article [80]. In the CVD method, temperature plays a major role in deciding the quality and the graphene grain size. It has been reported that depending on the temperature of annealing the graphene domain size can be altered. Several studies point to the structure and morphology of graphene overlayers as a function of annealing temperature and the amount of gas flow. All these have been summarized in a nice over view review article [9].

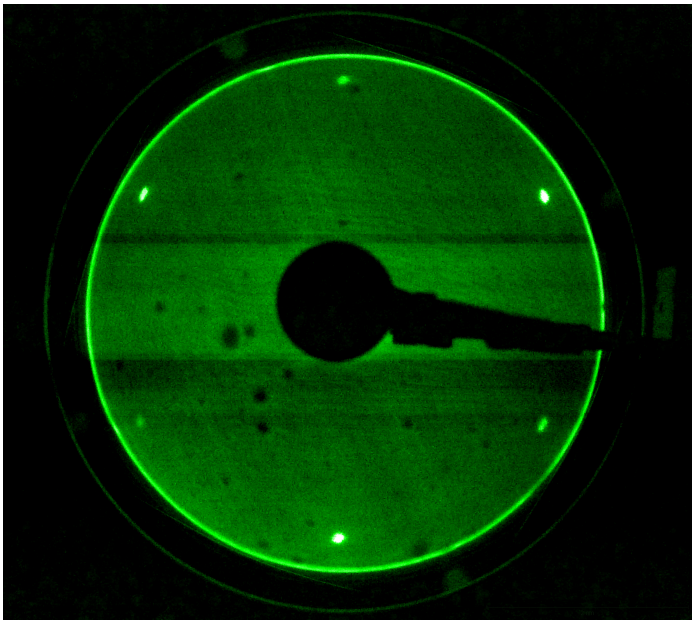

Figure 5.1.: cleaned platinum (111) in LEED. showing six spots. beam energy E= 70eV

5.2. Cleaning platinum

In order to grow pristine single layer graphene it is necessary to prepare an atomically cleaned substrate surface. Cleaning of metal Pt(111) surface from impurities are done by repeated annealing and sputtering with Ar^{+}ions . Most commonly observed impurities on bulk platinum are Silicon C, P, and Cl. Other impurities commonly observed on platinum include sulfur, chlorine and oxygen. Dissolved carbon segregates onto the surface upon heating 1170K [53]

Clean Pt(111) surfaces were prepared under UHV conditions. the cleaning process consists of involves recursive steps of heating and extended argon-ion bombardment (sputtering) till an atomically clean surface is obtained. By heating above 1200K platinum most of the carbon and silicon will segregate on the surface, subsequent sputtering removes the segregated impurities and any adsorbed molecules from the surface. The cleanness of the surface is tested with LEED and imaging with an AFM. In the first step the sample was heated to a temperature of 1273K and maintained at this temperature for 30 minutes and then sputtered with Ar^{+}ions

At higher annealing temperatures above 1273K the dissolved Silicon impurity

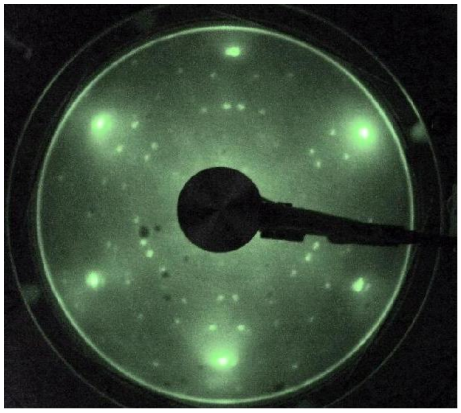

(a) LEED pattern indicating the growth of platinum silicide. beam energy was 72eV

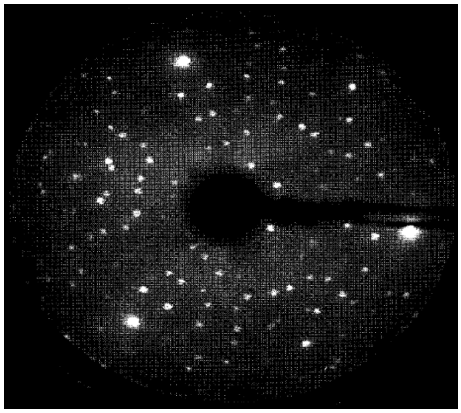

(b) LEED pattern of platinum silicide overlayer on Pt(111) from literature[18]

Figure 5.2.: LEED pattern recorded on Pt(111) upon extended heating shows the formation of platinum silicide. Silicon a major impurity in platinum which segregates on heating the sample to temperatures above 1273K for longer durations.

segregate from the bulk onto the surface and forms a thin layer of platinum silicide [18]. To get rid of this impurity, sputtering of the surface for longer duration (30min) is to be performed. Then the annealing temperature is reduced to 1173K. Sample was then heated to 1173K for 30minutes followed by quick sputtering at an elevated temperature (10 minutes). Usually 4-5 cycles of heating and sputtering will result in an atomically clean platinum surface.

5.3. CVD process-graphene synthesis

The CVD method has been successful in producing defect free graphene on metals. The chemical vapor deposition (CVD) method was employed where the sample was heated to a temperature of 1024K and then ethene was exposed on the surface for 120 seconds while maintaining the pressure in the chamber at around $5{\times}10^{-7}mbr$. Then the sample was let to cool down slowly to the room temperature. The temperature was monitored with the help of a pyrometer throughout the experiment. The coverage of graphene on the surface was hence confirmed with LEED and imaging in the AFM.

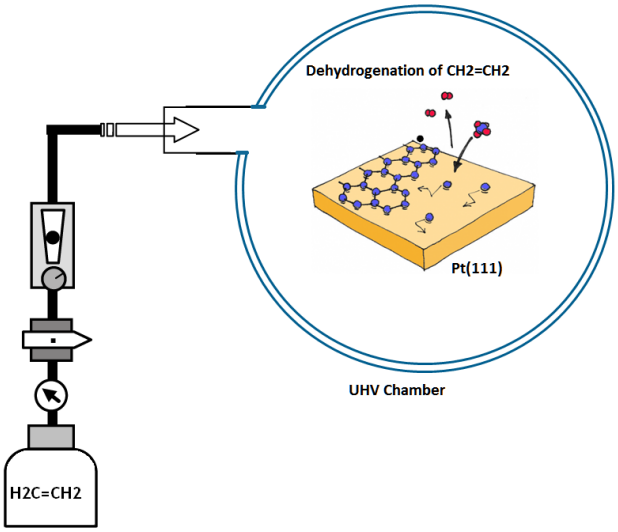

Figure 5.3.: Schematic picture of CVD synthesis of graphene on Pt(111) (Image source : http://www.nano.physik.uni-muenchen.de/research/rep11/index.html)

5.4. Growth of single layer graphene on Pt(111)

The nucleation growth process of graphene on metals from ethylene involves the following crucial steps steps: i) Dehydrogenation of ethylene and ii) Cluster formation of the released carbon atoms and iii) nucleation of carbon atoms onto the metal surface to form graphene. The second one may take place during the high-temperature period of the treatment or while cooling. Based on starting temperature configuration for ethylene decomposition, there are two distinct ways, (a) Making Ethylene to adsorb on the surface at room temperature and slowly heating up the metal surface higher than 1000K and again letting the sample to cool down in a slow pace. (b) Heating the sample to desired temperatures and introducing Ethylene on to the surface, and keeping the ow for some time (usually 2-3 minutes) then stopping the flow of gas and the controlled cooling of the metal surface. In the first routine Ethylene decomposition occurs around 500K followed by the intermediate step with the formation of CCH3 (ethylidene) a detailed mechanism is discussed in[67] [16]. In the latter one dehydrogenation takes place in the very early steps. Above 1173K, di-sigma- bonded ethylene dehydrogenates to ethylidene (M=CCH3) by transferring one hydrogen from one carbon to the other and losing hydrogen. The dehydrogena-

tion is accompanied by hydrogen atom recombination to H2, which then escapes as molecular hydrogen. We opted the second configuration for preparing graphene on platinum.

Growth rate of graphene is found to be nonlinear as the growth rate decreases upon increase in the graphene coverage and it also found not affected by the evolved hydrogen. It is because ethylene doesn't stick to graphene nor it decomposes on it. In this regard it is interesting to compare similar growth mechanism of graphene on other transition metals too [46], [14]. The temperature dependent size of the Graphene islands, grown with CVD method is discussed many a times and it is already observed that as the annealing temperature increases, much stronger diffusion of the surface carbon species occurs, leading to further growth of islands and attachment of the most islands to the step edges [39].

5.5. LEED on graphene

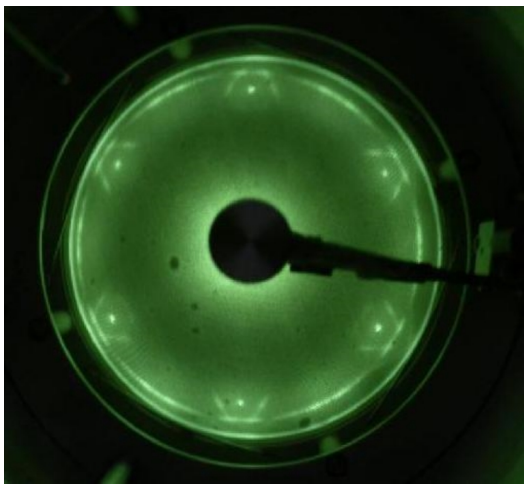

(a) LEED image on a graphene/Pt(111) system. After graphenising the surface of platinum the LEED image shows additionally a circular discrete ring and six satellite rings around the bright diffraction spots compared to the LEED image on bare platinum.

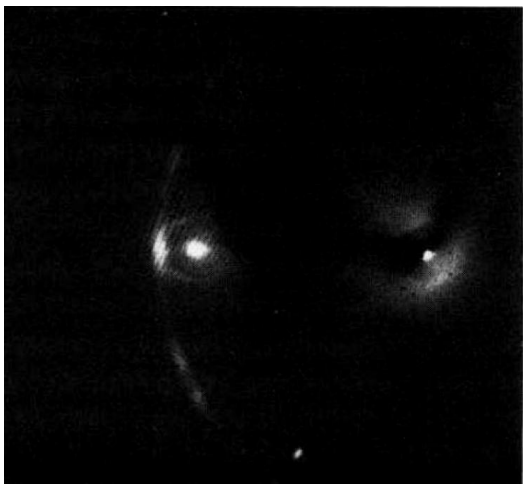

(b) LEED image Graphite overlayers/Pt(111) system from earlier literature. Appearance of satellite rings around the Pt(111) brighter spots can be observed similar to our LEED images on graphene/Pt(111) system.

Figure 5.4.: Low energy electron diffraction (LEED) pattern confirming the presence of graphene on the platinum surface.

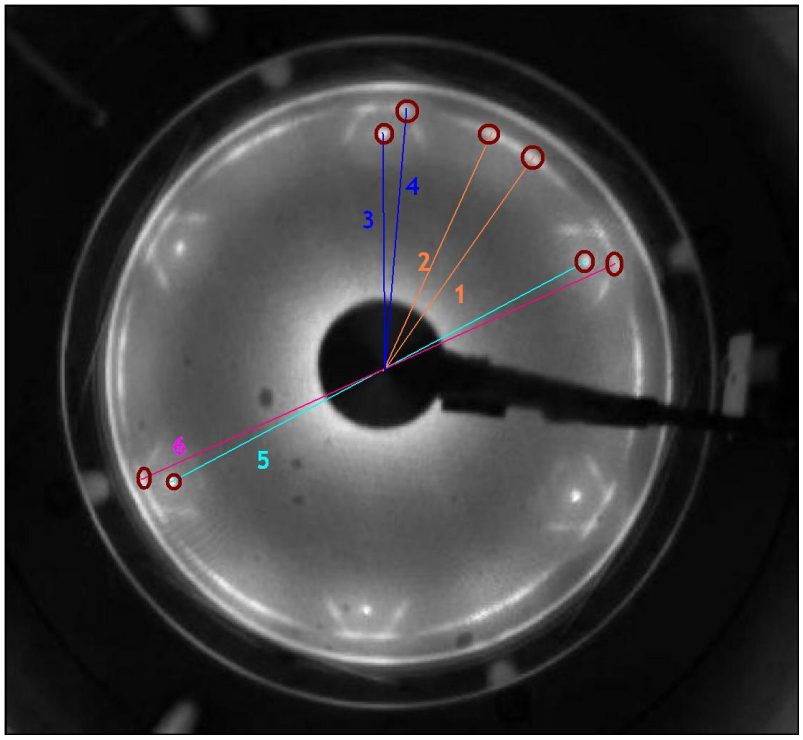

Figure 5.5.: Analysis of LEED pattern of graphene/Pt(111) system. Spots of interest are marked with red circles..

Graphene formation is confirmed by low energy electron diffraction (LEED)5.4. Low energy electron diffraction (LEED) pattern confirms the presence of graphene on the platinum surface. The LEED image shows six brighter spots arising from the substrate lattice platinum. Additional satellite rings around the brighter spots indicates that the graphene has different rotational domains[82] on the platinum surface. In an earlier work [82] LEED images of incommensurate graphite overlayers on Pt(111) has been thoroughly discussed. The figure figure 5.4b shows the similarities with our LEED images on graphene/Pt(111) and LEED image from the literature. Presence of graphene domains in the form of patches oriented at different directions were were imaged in contact as well as non contact atomic force microscopy which will be discussed in the next chapter.

The figure 5.5 show the analysis of the LEED pattern obtained on graphene/Pt(111) system in our preparations. The six brighter spots are from the platinum surface. The outer ring has a higher diameter than the distance between the two opposite

brighter spots from platinum surface (line 5 and line 6). This is because of the lattice constant of the overlying graphene (0.246nm) is smaller than the platinum(111) (0.775nm). The ratio between the lattice constants of graphene and platinum is 1.125 which is in good agreement with the ratio calculated from the LEED image. In addition to this, the pair of spots on the outer ring between the brighter spots are due to the existence of two main different rotational patches of graphene. These spots corresponds to two rotational mismatches of 23.4° and 36.3° (angle between [3 and 1] and [3 and 2]). Other relative orientation of graphene found to be is 4.6° (angle between lines 3 and 4). The angle between the different patches with respect to the platinum lattice is calculated to be 4.6°, 23.4° and 36.3° (see the line 3 and 4).

6. Imaging of graphene

Graphene layers on metal surfaces have been attracting the attention of scientists since several decades. Some studies of the catalytic action of closely packed transition metal surfaces during mid 60's reported the formation of graphitic overlayers on the surface [29, 27, 40]. At present graphene growth on metal surfaces via surface segregation or decomposition of hydrocarbons on the surface is considered to be the most promising way to prepare large defect-free areas of graphene [80, 4, 75]. These graphene layers can be transferred to other surfaces and used for engineering applications.

In this chapter we present images of graphene on a Pt(111) substrate which was grown by CVD synthesis. We employed noncontact AFM, Scanning Tunneling Microscopy (STM) and combined STM/AFM modes for imaging the graphene surface. Before moving to the experimental results we present a brief introduction of STM and combined STM/AFM imaging modes.

6.1. STM

In the early 1980's two IBM scientists, Binnig & Rohrer, developed a new technique based on the concept of quantum tunneling for studying surface structures, called Scanning Tunneling Microscopy (STM). The development of the technique was an important breakthrough in the field of surface science. The principle of operation is based on the detection of tunneling current between a sharp metallic tip and a conducting surface. When a conductive tip is brought very near to the conductive surface under study and a bias voltage is applied between the tip and the sam-

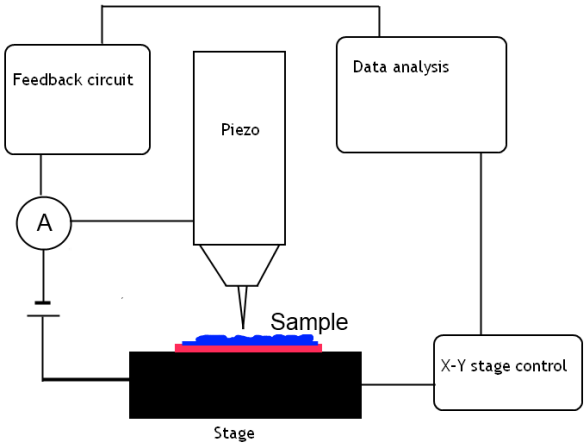

Figure 6.1.: Schematic diagram of STM operation.

ple, electrons can tunnel through the vacuum between them. Figure.6.1 shows the schematic diagram of a Scanning Tunneling Microscope setup . Tunneling currents are usually in the picoampere to nanoampere range. This tunneling current is a function of local density of states (LDOS) of the sample, tip sample distance and the applied voltage. STM can be operated in two modes [13] 1) Constant height mode or 2) constant current mode.

In constant height mode, images are acquired by just measuring the tunneling current while the tip scans on the surface at a constant height. Constant current mode is the most frequently used mode of STM. In this mode the tip-sample height is varied in order to maintain a constant tunneling current. STM requires extremely clean and stable surfaces, sharp tips, and vibration isolation. Since conductive sample and tip are the prerequisites, STM technique is only applicable for conductive samples. STM achieves atomic resolution imaging of conductive surfaces very easily compared to other AFM techniques.

6.2. Combined STM/AFM mode

In the noncontact AFM mode, a cantilever is oscillated at its resonant frequency and the amplitude of this oscillation is set to a desired value. When the cantilever scans

over the sample surface, the distance between the tip and the sample is controlled by observing changes in the oscillation frequency or changes in the oscillation amplitude of the cantilever. These changes are due to the attractive interaction between the atoms at the tip and the sample. In the combined STM/AFM mode, the first few frames are captured in the constant current STM mode and after a stable imaging is achieved, the tip sample distance control is switched to frequency modulated AFM while recording the tunneling current simultaneously. Images acquired in this mode give much more information about the surface morphology and the electronic structure of the surface at the same time. In addition to the noncontact mode imaging, we have also imaged graphene/Pt(111) in this mode and the images are presented in the next section.

6.3. Results

First, an atomically clean platinum surface was prepared and the cleanness is confirmed via LEED (figure 5.4) and imaging in noncontact mode AFM. Then the surface was graphenised by CVD synthesis. The quality of graphene is found to be greatly dependent on several factors [46] in CVD synthesis, like annealing temperature, duration of ethylene flux, rate of cooling etc. CVD growth of graphene on transition metals under a very wide range of experimental conditions are discussed in the review article by Biro et al. [9]. Since the growth dynamics of carbon deposition is not completely known, finding the proper balance of such parameters is a largely an experimental task [28]. All STM/NC-AFM images presented here were collected at room temperature using OMICRON's VT AFM. An atomically clean surface of Pt(111) looks like in Fig. 6.2. Platinum substrate steps are mostly parallel to each other and extend over several micrometers. The images are recorded in nc-AFM mode with a silicon cantilever of nominal stiffness$\approx 40N/m$.

The platinum surface was covered with graphene by CVD synthesis. Ethene was decomposed on the surface at $900^{\circ}C$. LEED analysis of the surface confirmed the formation of the graphitic overlayer. Further imaging of the surface in nc-AFM in-

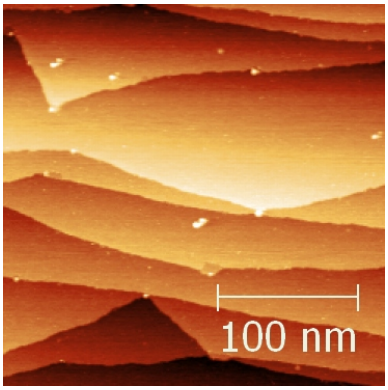

Figure 6.2.: Atomically clean surface of Pt(111) recorded in nc-AFM mode with a frequency shift of - $\triangle f = -66Hz$ and amplitude = 10nm

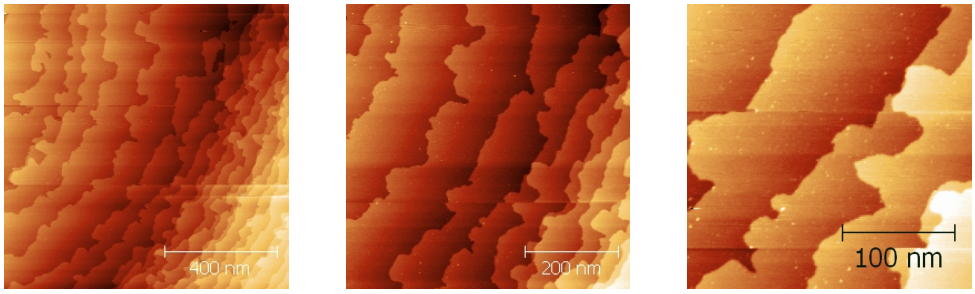

(a) (b) (c)

Figure 6.3.: Noncontact mode AFM images of graphenised Pt(111). The step edges of the platinum are altered due the carbon nucleation. Three images with different scales show how the formation of graphene changes the morphology of platinum surface.

dicated the presence of graphene as alteration in the shape of step edges of platinum (see figure 6.3). Clean platinum shows almost parallel and straight step edges, but after graphenising the surface the platinum step edges become zig-zag in shape. This is due to the fact that the carbon nucleation always starts at the step edges of platinum. The platinum atoms diffuse at high temperatures and also during the nucleation growth of graphene. As the sample cools down after a CVD process from very high temperatures, the mismatch in thermal expansion coefficients between Pt ($8.8 \times 10^{-6} K^{-1}$) and graphene ($>1 \times 10^{-6} K^{-1}$) leads to a building up of compressive stress in the graphene sheets. This stress is relaxed elastically by the formation of wrinkles or folds in the graphene [7, 60]. The images (Figures 6.4a and 6.4b) exhibit graphene wrinkles extending over several hundred nanometers.

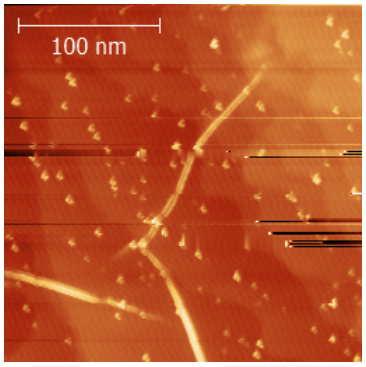

(a) nc-AFM image on the graphene/Pt(111) showing the wrinkles. Graphene modified step edges of platinum are also observed in the background.

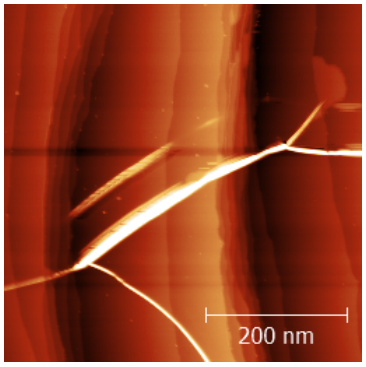

(b) nc-AFM image of graphene/Pt(111) showing the wrinkles

Figure 6.4.: Figures (a) and (b) shows graphene surface with wrinkles extending over several hundred nanometers

6.4. Moiré patterns on graphene

The graphene forms Moiré superstructures due to lattice mismatch and misorientation between graphene and metal substrates. The Moire superstructures of graphene have been reported for many metal substrates. The lattice mismatch between graphene and the Pt(111) substrate leads to the spatially periodic electronic structure.

In most of our preparations we observed multi-domain graphene separated by grain boundaries of amorphous carbon [9]. The figures 6.5 show a larger scan area of $(30 \times 30) nm^2$ recorded in contact mode. The friction forces on the patches and at the step edges are almost the same which speaks for a continuous coverage of graphene on the Pt(111) surface.Also one of the the graphene patches (boundary marked with the black line) is continuous and extends across the platinum step which is an other proof for the continuous graphene coverage. We studied morphology and structure in noncontact mode and the combined STM/AFM mode. Figures (6.6a) and (6.6b) show images where several domains are imaged together with atomic resolution. The low energy electron diffraction (LEED) pattern (see figure (5.4)) shows a satellite ring structure indicating that many different orientations of graphene are present.

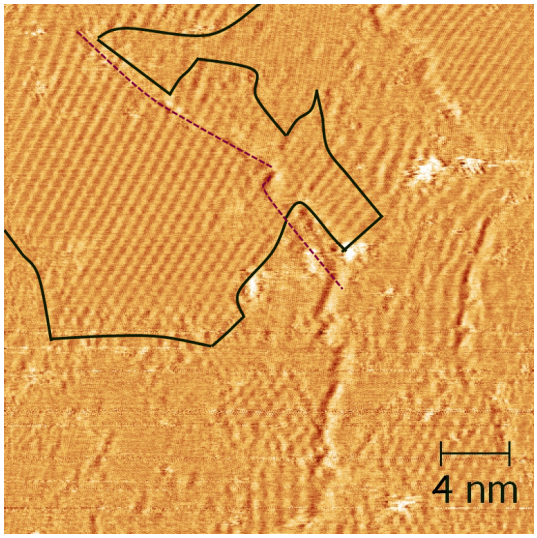

Figure 6.5.: Moire superstructers of different periodicities on graphene/Pt(111) in Contact mode.

Moiré periodicity is found to vary from $0.2nm$ to $1.2nm$ depending on the relative orientation between graphene and Pt(111).

Figure 6.6b shows a high resolution STM image on one of the graphene patches. The hexagonal periodicity observed for the overlying graphene in this image is about 0.24nm. The large unit cell arises from the the superposition of the misoriented lattices of graphite and Pt(111) substrate. By observing the real space image and its 2D Fourier transform (see Figure 6.7), we find that the superstructure is a$(\sqrt{19} \times \sqrt{19})R23.4°$ unit cell with respect to the graphite lattice [21]. Exact rotational mismatch between graphene and the Pt(111) is not directly accessible from the LEED images but it can be calculated analytically by simple models. A method for calculating the rotational mismatch between graphene on an hexagonally arranged lattice has been described in [81]. This method takes the moire periodicity and the known lattice constants of Pt(111) and graphene as inputs to calculate the misorientation angle.

The large scan area image of graphene/Pt(111) (see fig 6.6a) with STM/AFM imaging mode clearly shows that the graphene has many other orientations, too. In most of the STM experiments on graphene it is most likely that the tip comes into contact with the graphene layer. But in our STM/AFM experiments it is almost

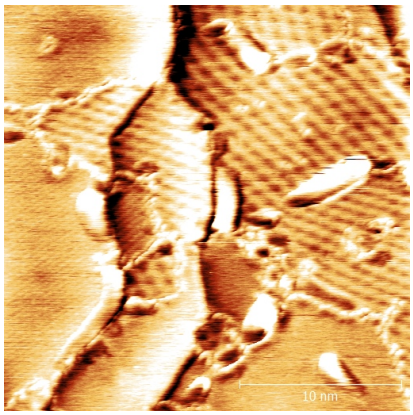

(a) High resolution image on graphene/Pt(111) in a combined STM/AFM mode.

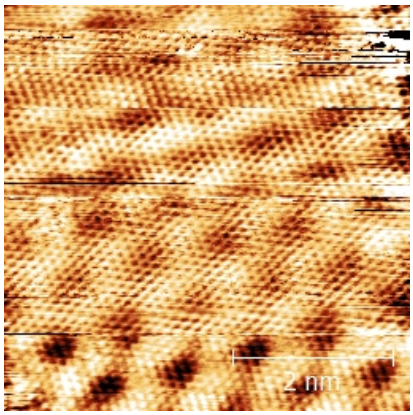

(b) STM image at constant current mode of graphene/Pt(111) V_{bias}= 0.405V. Both graphene and the Moire superstructure are well resolved. Image size is $(10 \times 10)nm^2$

Figure 6.6.: Multidomain graphene on Pt(111) images with noncontact and combined STM/AFM modes. Different graphene domains are separated by grain boundaries (GB).

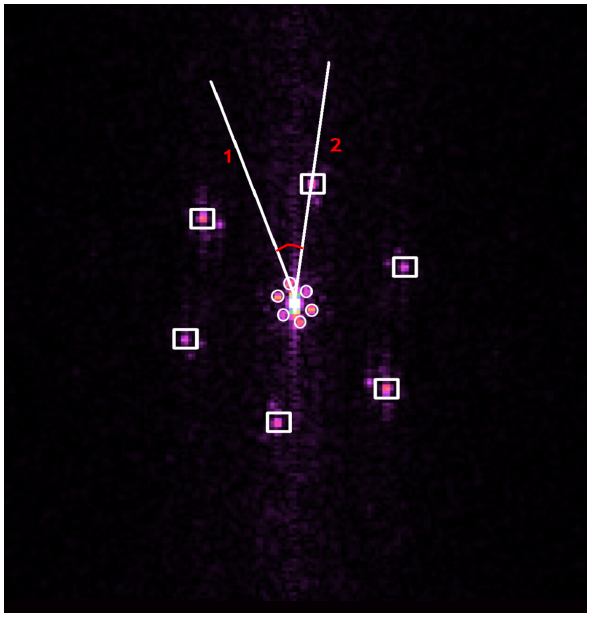

Figure 6.7.: Fourier transform of image 6.6b, showing the graphene lattice periodicity of 0.25 nm marked by squares, and the moire´ superstructure periodicity of 0.78 nm marked by circles. The angle of rotation of the superstructure is found to be 23.4°

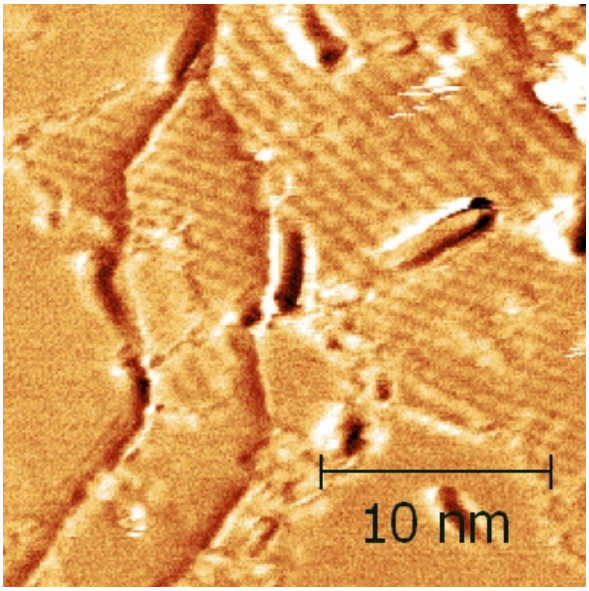

Figure 6.8.: Excitation data on the small scan area as shown in the figure 6.6a.

impossible that the tip comes into contact with the graphene surface. Suppose if the tip comes in contact with the graphene, then there should be a huge drop in the resonant frequency of the cantilever which we have never encountered. High resolution imaging in STM/AFM of a large scan area of graphene/Pt(111) in fig6.6a clearly show different Moire corrugation of graphene patches. The excitation channel which indicates the energy dissipated or the energy spent to keep the cantilever amplitude constant provides additional information about these patches, see Fig 6.8. A difference in the excitation value of 12.2% was observed between the two patches of high and low Moiré periodicity. The the energy dissipation is higher on Moire corrugations which has higher periodicity.

7. Load dependent friction tests on graphene/Pt(111)

Graphene a two-dimensional material exhibits unique friction and wear properties. Carbon coatings like DLC are often used to achieve very low friction and also to improve the lifetime of machinery parts [20, 37, 45]. There are many recent reports on the mechanical properties of graphene layers. Graphene could reduce potential damage to the surfaces in contact at the same time it reduces adhesion and friction in nanomechanical and microelectromechanical systems (MEMS)[48]. It is worth to mention some of the previous studies on the wear and frictional properties of graphene on different substrate materials including metals [59]. Friction and dissipation on single layer and bilayer graphene in graphene/SiC system have been compared and it was reported that the friction on single layer is higher than the double layer [25][24]. Friction reduction on graphene layers and a deviation in frictional magnitude between graphene layers of different thickness has been reported on a SiO_2 surface[43]. The effects of repetitive scanning on friction and wear on single layer graphene epitaxially grown on SiC at the micrometer scale have been studied by Marchetto et al. [47].

Extreme mechanical strength is the reason for graphene being a wear resistive material. Lee et al.[42] examined the elastic stiffness and frictional properties of graphene and confirmed it to be one of the strongest materials ever measured. In this study graphene was suspended over a substrate with micron-sized circular holes, and indented by an AFM tip. By fitting of the force-distance curves from the indentation tests, gives the elastic stiffness of graphene. The measured strength of a

graphene sheet was found to correspond to a Young's modulus of 1 TPa. Graphene's unique mechanical properties make it a promising candidate for the tribological applications where control of friction and wear are major criteria. Much about the stability of graphene as a wear resistive coating is unknown. We have focused on the experimental characterization of graphene's mechanical stability when used as a surface protective layer.

The work presented here is based on results presented in the publication [36]. Our load dependent friction experiments are carried out in order to verify the findings of a simulation of the mechanical properties of the graphene/Pt(111) system. Graphene is a potential solid lubricant for many tribological systems where metallic contacts are employed. An interesting question would be: "How well can graphene act as a wear resistive lubricant?", simulation work carried out by our collaborators have addressed this question by simulating nanoscratch and nanoindentation experiments on graphene/Pt system. Simulation on graphene/Pt(111) are done by employing realistic potentials and realistic interaction models. A short description of simulation method and results are presented here.

In the simulations, for investigating the response for different tip roughness, two tips with different geometries are used, a smooth and a rough tip of three different tip radii 1.5nm , 3.0nm , and 5.0nm 7.1. The results presented here are only for the tip of radius 3.0 nm because the tip used in the experimental study compares well with this tip radius. The Pt(111) is a cube with a side length of around five times the tip radius. Van der Waals forces between graphene layer and substrate are modeled with a Pt−C Lennard-Jones potential. The tip velocity for indentation and nanoscratch experiments is $0.1\mathring{A}$ per second. Simulation of mechanical tests on graphene when the graphene flake was pinned to the surface, and a flake freely attached to the surface are also modeled.

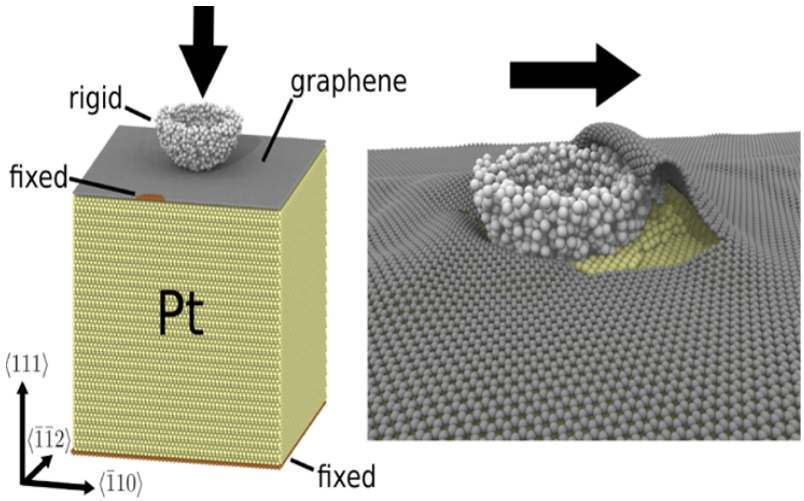

Figure 7.1.: Simulation set up

7.1. Simulation results by Andreas Klemenz et al.

By the results of indentation simulation here, shows that the forces required in order achieve same penetration depth on bare metal are much lower compared for the graphene covered metal. Graphene coverage hence significantly improves the load bearing capacity of metal. Simulation of nanoindentation recognizes three distinct regimes of indentation:

1. Hertzian regime - elastic deformation
2. Plastic deformation of substrate
3. Graphene rupture regime.

The simulation of nanoscratches, aims at the frictional behavior in the above three regimes. The simultaion was performed for constant penetration depths unlike the experiment where the nanoscratch experiment was performed for constant force. Therefore we see a cotuinuous load dependence in the plot 7.2 .The plot 7.2 depicts the configuration of tip and sample at the three regimes with the corresponding friction trace in the nanoscratch test .

A plot of friction force F_f versus normal load F_N in Fig.7.3 displays the friction in the different regimes mentioned above. At low loads sliding is almost frictionless and

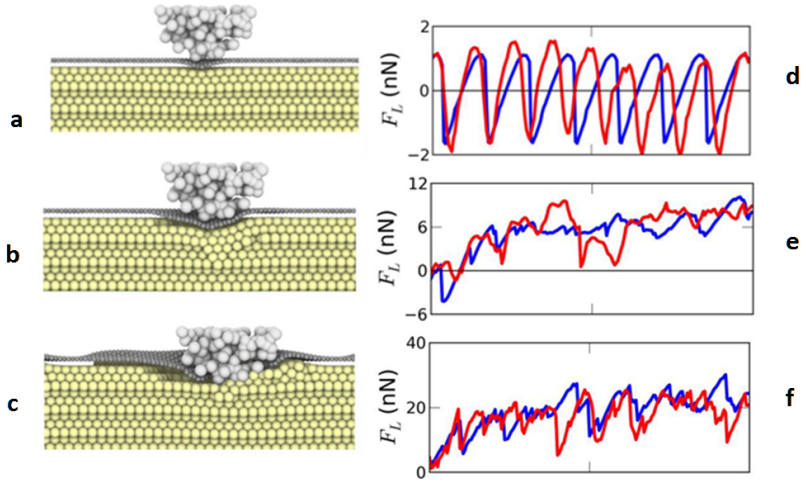

Figure 7.2.: Simulation of scratching with amorphous indenter. At low normal forces the substrates deform elastically, the lateral forces are low and show stick−slip behavior. When the substrates deform plastically under the intact graphene layer, the lateral forces increase and and the stick−slip pattern disappears .Finally at high loads graphene ruptures and strong plastic deformation and formation of wear tracks follows. Friction jumps are drastic after graphene failure.

the characteristic stick slip behavior was observed in the lateral force traces (7.2 d). Upon increasing the force around ≥100nN, the substrate under the graphene starts to deform plastically but the friction doesn't change significantly. For forces above $100nN$, the platinum under the graphene deforms plastically (red symbols) and the stick slip behavior disappears with a slight increase in the friction force. For sliding at forces above $210nN$, a sudden jump in the friction was observed which is one order magnitude higher than the friction force observed at previous loads. Here the friction force measured is equal to the friction on bare platinum (point where green and yellow symbols meet), which is an indication for the graphene rupture. raphene fails to protect the underlying substrate and immediately undergoes rupture. In order to compare the benefit of having graphene on top of metal, simulation of similar scratch and indentation studies on bare metal surface were performed. Almost no friction region is observed on bare platinum, for very low loads compared to graphene covered case and friction increases linearly with the load.

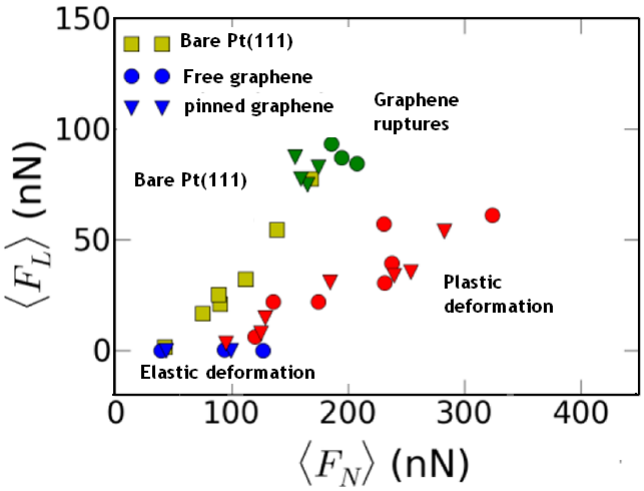

Figure 7.3.: A plot from simulation results showing the relation ship between friction force F_f and applied load $F_N$on bare graphene, Pt(111) covered with graphene. Data points for the bare substrates are shown with yellow symbols. Blue and red symbols represent elastic and plastic substrate deformations under an intact graphene layer, respectively. Green symbols represent graphene ruptures regime.

7.2. Experimental results

This section discusses our experimental findings on the mechanical stability of graphene on Pt(111) under high stresses. High stress conditions occur in real time applications are studied with the help of an AFM in an ultra high vacuum environment at room temperature. Friction and mechanical stability of graphene are measured as a function of loading force. The experimental results of load dependent tests are described in two subsections. The first subsection shows the scratch tests results performed with a stiffer silicon cantilever and the second section contains the results of load dependent friction tests carried out with a diamond coated softer contact mode cantilever.

Two schemes are adopted for the scratch test (see Fig. figure 7.4) 1) A recursive line scan along a fixed position with increasing load 2) A frame scan, where the tip scans over a frame and the load was gradually increased from bottom to top of the frame. For our load dependent friction experiments on graphene we employed two diamond coated cantilevers with different force constants. The first one was shorter

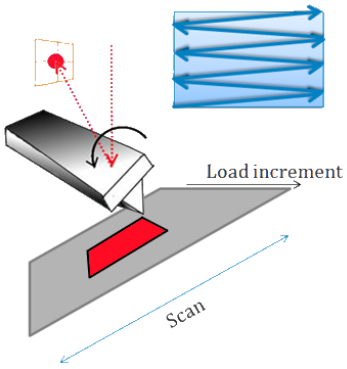

(a) Frame scan with increasing load from bottom to top.

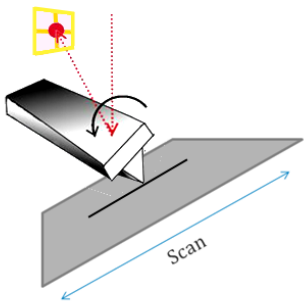

(b) Line scan where the scanning was performed back and forth along a line of length 100nm (256 runs with 256 data point fro each line). The load values changed after each cycle.

Figure 7.4.: Two different experimental design of load dependent friction measurement.

cantilever of stiffness ≈42N/m suitable for dynamic mode and another one is a soft contact mode cantilever with a stiffness of ≈1N/m.

7.2.1. Scratch test with a stiffer cantilever

First we to measured the load required to create a wear track in a graphene sheet on Pt(111). For this experiment we used a diamond coated silicon cantilever of stiffness ≈42N/m (DT-NCLR from Nanosensors). A single line of length $400nm$ was scratched at the center of the scan area with different loads. The sample was imaged in contact mode in between each scratch test. The Sample was scratched with different normal loads of F_N=12µN and F_N=16.5µN at a velocity of 100nm/sec. Scratching with these loads did not produce any wear. Then as a further step, we made two line scratches of 400nm length with 20 runs at higher loads of 16.8µN and 23.5µN , see Fig 7.5 . In the post images of the surface recorded in contact mode, we observed two wear tracks which were produced by scratching at the two loads 16.8µN and 23.5µN. A rough estimate for the contact pressure to create wear on the graphene is calculated as 1GPa.

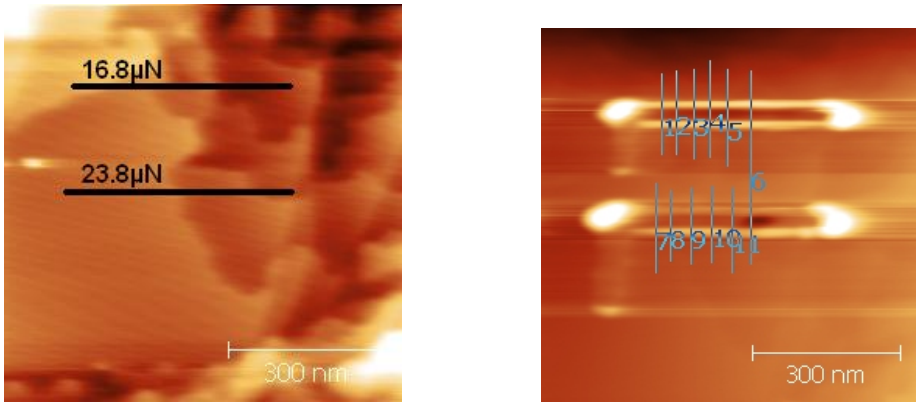

(a) Proposed line scratches on graphene/Pt(111)

(b) Post image around the line scan

Figure 7.5.: *a*) Topography image showing the surface structure before scratching. and *b*) The line along which wear is done, wear tracks produced in the course of scratching.

$$\frac{F_N}{A} = \frac{16.8\mu N}{2\pi(50nm)^2} \approx 1GPa$$

The tip contact radius of approximately 50 nm deduced from wthe width of the wear track

In the next experiment graphene was scratched at ten different sites. Line scratches of $100nm$ length at fixed velocity of $100nm/sec$, with varying loads starting from $2.1\mu N$ to $23.5\mu N$ were made. (see Figure 7.6). Wear of the graphene layer sets on upon scratching at load $16.8\mu N$.

To reveal the exact load at which wear of graphene commences, further six different line scratches were made with loads starting $16.8\mu N$ to $23.8\mu N$. Figure 7.7shows that a clear wear track is produced after loading at $16.8\mu N$ of force. As we can see here in the first set of experiment a load of $16.8\mu N$ did not produce any wear but in the next set of experiment with six loads it is clear that wear started at $16.8\mu N$ the reason for this could be the relative sharpening of the tip after the first set of measurement.

(a) Image of the scan area where the ten line scratches of different loads were proposed.

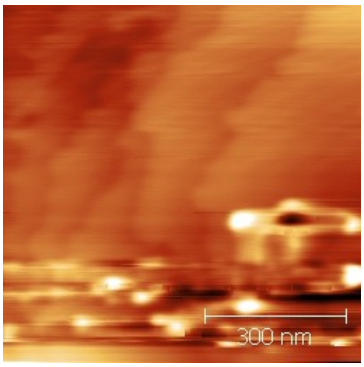

(b) Post image in contact mode showing the wear tracks produced for the three highest load values.

Figure 7.6.: Ten line scans of various loading forces were made on surface of graphene/Pt(111) to determine the necessary load to required to brak the graphene layer.

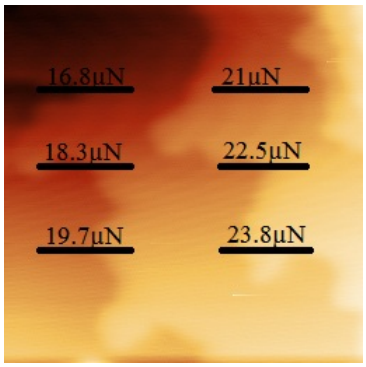

(a) Previous image of the scan area where the six line scratches of different loads were proposed.

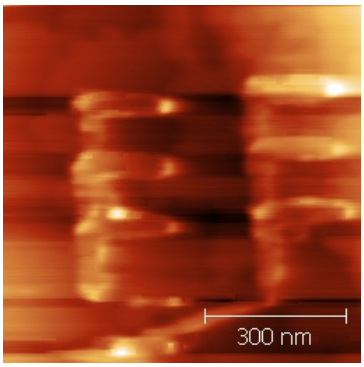

(b) Post image in contact mode showing that the wear tracks produced for all the load values.

Figure 7.7.: a) Position of six scratches with load ranging from 16.8µN to 23.8µN. b) wear tracks are produced after loading at 16.8µN of force.

7.2.2. Load dependent friction tests with a soft cantilever

The measurement of friction force in a nanoscratch test on graphene using an AFM requires the sensitivity of a soft contact mode cantilever. In this set of experiments, graphene on Pt(111) was subjected to a load dependent scratch test by employing a soft diamond coated cantilever (dimensions: length 450µm, width 50µm) with a nominal stiffness around $1N/m$. The mechanical properties of graphene on Pt(111) were studied by high-resolution atomic force microscopy (AFM) in UHV. Line scans of varying load were carried out as follows, 256 runs on a scan line of length 100nm with 256 data points were recorded on each line where the loading force was increase from zero to $400nN$ in smaller steps of 5nN. In case of frame scans, a scan frame is captured comprising of 256 lines with 256 data points for each line but the load value was increased systematically from bottom to top of the scan frame. The average friction values for forces were calculated by subtracting the average value of forward and backward scans in a cropped scan frame to exclude effects of directional change. A schematic diagram below depicts the routine of our load dependent friction measurements in case of frame scans.

In our experiments an area where a graphene extends relatively large area is selected . The tip radius was estimated from the widths of wear tracks to be about $2.4nm$. The very tip apex is probably formed by a crystalline corner. Load dependent friction values for a line scan of length 100 nm fall into four regimes of elastic deformation, plastic deformation of Pt below the intact graphene, sliding while rupturing graphene, and sliding after graphene is ruptured. The results of friction force F_f versus normal $F_N$load is shown in the figure 7.9 and all these four regimes are labeled in the Figure.. Sliding at very low normal loads till ≈70nN showed almost no friction (friction coefficient ≈ 0.0003). Figure 7.10b shows a characteristic stick slip behavior observed for sliding at low load regime and allows a direct comparison with the observed stick slip in the simulation (see Fig.7.2 d). Upto a normal load of $120nN$, the friction force was almost negligible,however when the load was $\geq 50nN$ small spikes in friction forces appear momentarily but again a low friction regime

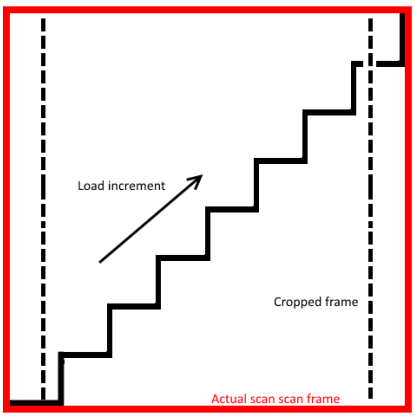

(a) Schematic diagram of experimental routine of load dependent friction measurements´in a frame scan scheme. The outer square in red color is the actual scan frame measured and the inner box (dotted) is the cropped frame, showing the area in the imge used to extract friction forward and backward data excluding effects of directional change. Inset stepped black line indicates how the load was changed during the scan. Once a load is incremented the that load was held for few scan lines ($\approx$ 4 lines).

(b) Schematic diagram of experimental routine of load dependent friction measurement in a line scan scheme. The black line displays a line scan. 256 scans on this line with an increasing load from zeo to 400nN was performed. Once a load is incremented the that load was held for few scan lines ($\approx$ 4 lines). The red box on the line shows the portion of the image from where the data is considered for analysis.

Figure 7.8.: Two adopted experimental schemes. a) Frame scan b) Line scan

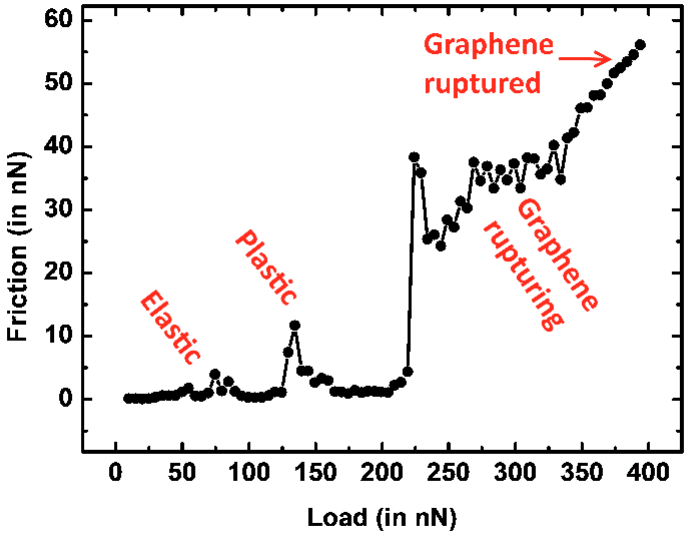

Figure 7.9.: Graph of normal load F_N versus friction force F_f. Average friction versus load for a scan range of 100 nm, each data point corresponding to average in four subsequent scan lines. The four different regimes of elastic deformation, plastic deformation of Pt below the intact graphene, sliding while rupturing graphene, and sliding after graphene is ruptured are labeled.

is observed upon increasing the load . For normal loads around 50 nN, in the simulations for the predicted the coexistence of elastic sliding and plastic deformation of Pt below the graphene Fig.7.3. This can explain the friction spikes observed in our experiments. After a loading force around $220nN$ the friction shows a sudden increase and the transition from low friction to high friction regime is discontinuous. For the higher loads between $210nN$ and $330nN$, we observed a regime of unstable friction, but after the load $330nN$ and higher the friction varies linearly with the load indication clearly the rupture of graphene.

In the elastic regime the friction force microscopy of graphene reveals the surface structure through stick−slip motion. The periodicity of stick−slip is defined by the honeycomb structure, additionally modulated in a Moiré pattern caused by the difference in lattice constants and orientation between Pt(111) and graphene (see Fig.7.10a). Several patches of graphene exhibiting different in the Moiré periodicites

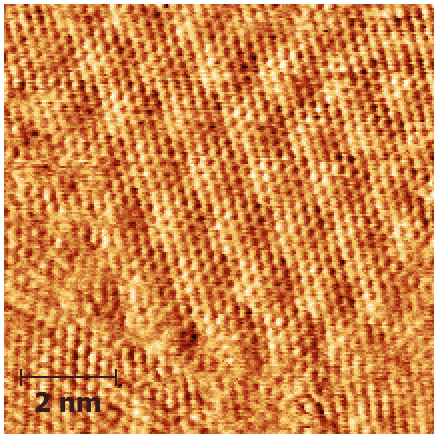

(a) FFM image on graphene/Pt(111) for normal load 10nN. Image shows stick atomic resolution through stick-slip motion corrugated by the Moire pattern

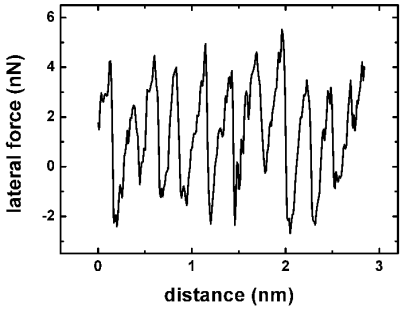

(b) Lateral force as a function of distance showing the typical sawtooth characteristic of atomic stick—slip

Figure 7.10.: High resolution lateral force image on the graphene/Pt(111)

are also observed. As seen in the last chapter, Moiré superstructure can be imaged in both noncontact and contact modes of AFM. Figure 7.10a was recorded in contact mode with very low normal load ($\approx 10nN$). This image shows the graphene lattice and also Moire corrugation. At the bottom left corner we could see a different periodicity on Moire this is because of an another graphene patch which is has a different orientation. Both the graphene lattice and the superstructure are clearly resolved in the image. Therefore in the low load sliding regime we have seen a clear stick-slip behavior modulated by Moiré corrugation.

We have investigated the changes that occur in the plastic deformation regime. The load dependent friction experiment was halted after the appearance of first friction spike and the topography of the surface was imaged in high resolution friction force microscopy. FFM images shows the formation of isolated round hillocks of about 1 nm height (see figure 7.11a). High resolution lateral force imaging of the hillocks and the surrounding area clearly shows that the graphene layer is intact even after the friction spikes. Moire corrugation of the graphene layer is still visible on the hillocks and the friction on these hillocks is not significantly different than on the surrounding terraces but only slightly modulated by the topographic effects.

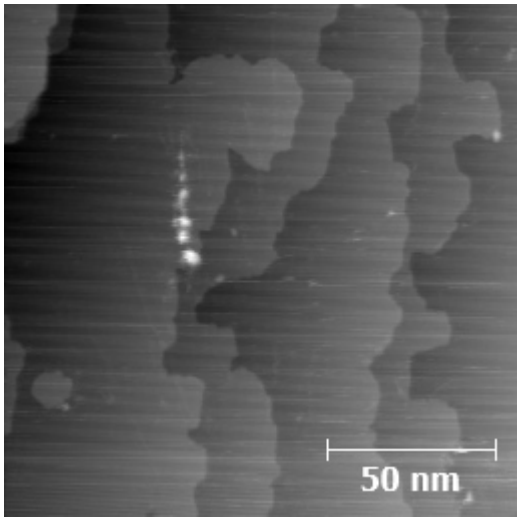

(a) Topography of the surface where the load dependent line scan measurement was done. Formation of hillocks exactly at the location of scratch test are visible.

Figure 7.11.: AFM image of topography showing the formation of hillocks exactly at the load dependent line scan experiment was carried out.

These two factors confirm that the graphene layer stays intact in the plastic regime (Figure(7.12b)).

In our experiments, the load required to apply in order to create wear on graphene with a stiffer cantilever was found to be three orders of magnitude higher than for the soft cantilever. This differences is obviously by the sharpness difference between the two tips. We conclude that, at the applied breaking force the pressures under

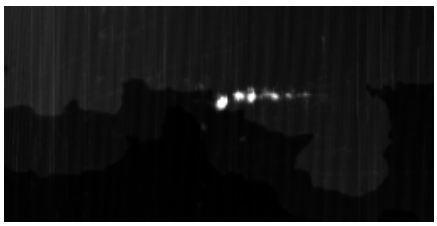

(a) Zoom in image into the topography of hillocks (frame size 300 nm × 150 nm).

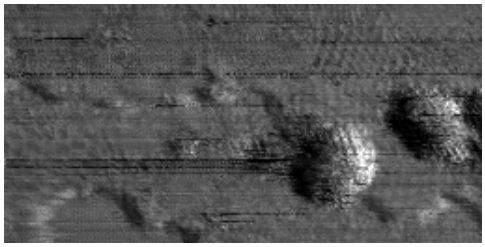

(b) High resolution lateral force image of two leftmost hillocks (frame size 60 nm × 30 nm). Friction on the hillocks is not significantly different from compared to the surrounding terraces and only slightly modulated by topographic effects.

Figure 7.12.: High resolution lateral force image on the graphene/Pt(111)

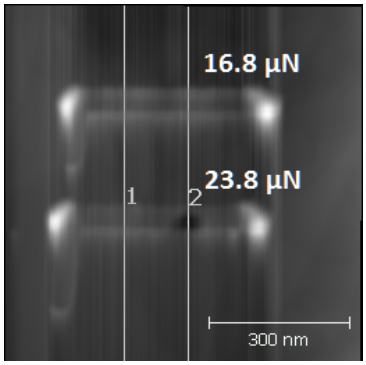

(a) Two wear tracks formed at the loads

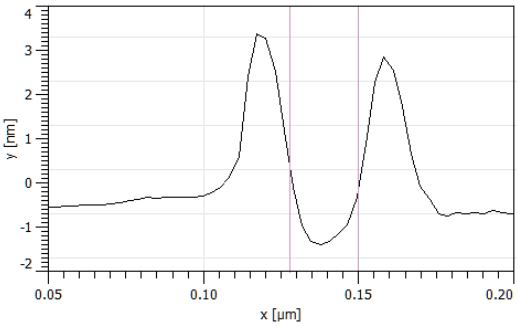

(b) Line profile across the first wear track

Figure 7.13.: Estimation of the tip radius from wear tracks.

the both the tips were almost the same.

The Pressure under the tip at breaking loads for the two tip radii are calculated from their respective scratch profiles. A line profile across the wear tracks give an estimation of the tip radius and hence the contact area. For the first tip (stiffer) the contact area is about $22nm$ this resulting a contact area of $759.88\times10^{-18}\ m^2$. The calculated pressure ($\frac{F}{A}$) is about $2.105\times10^{10}N/m^2$. The Tip radius for the soft cantilever is $2.4nm$ which is one order magnitude smaller than the stiffer cantilever. Comparatively, a low load was sufficient to break the graphene for the softer cantilever. The load at which graphene ruptured was around $210nN$, the corresponding pressure under the tip at this load is found to be $2.261 \times 10^{10}N/m^2$. Pressures are found to be in good agreement between the two tips and breaking pressure is independent of tip geometry.

7.3. Discussion

Nanotribologcial studies of graphene have shown the graphene's excellent potential as solid lubricant, with limitation in wear resistance. We have presented experimental results that are in very good agreement with the findings of nanoscratch tests in simulations . Simulations of nanoscratching predicted three sliding regimes. For a tip of $3nm$ radius, sliding at loads from zero to $200nN$ is almost frictionless (Friction coefficient $\mu < 0.003$) and the deformation of the graphene is elastic and

follows Hertz's law till a load of $100nN$. In the experiments we have observed few high frictional spikes at around $50nN$ but they disappeared upon continued sliding with increased load and the system returned to the low friction state. Reason for friction spikes is possibly because of a local strain hardening of the Pt in the region around the plastically deformed site and the simulation predicts a co-existences of low friction sliding with plastic deformation of Pt. The third regime starts when the graphene ruptures just starts. In this regime friction values show fluctuations, because, at this loads the tip slides on the Platinum with ruptured graphene attached. After $330nN$ the friction response is linear with the load. Compared to the friction values on bare platinum we concluded that sliding above load of $330nN$ it is completely plowing on the Platinum and graphene is completely ruptured. In the experiments we have shown that the pressures at the tip for for breaking graphene is independent of tip geometry. A sharp tip of $2.5nm$ breaks the graphene at very small load around 200nN but for a tip of $22nm$ radius it takes $17\mu N$ to break the graphene in both the cases pressures at the tip was almost the same. The results show that graphene is an excellent coating for low friction and wear, but provided that coating itself is not damaged. Graphene is ideally the best candidate as lubricant and a wear protective coating at low load scenarios. on metals at low loads Once the graphene ruptures it loses its low friction and wear properties.

Part IV.

Conclusions and Outlook

Friction is ubiquitous in nature: it occurs when two surfaces come in contact and move relatively. A major portion of the energy produced is spent to overcome the friction in all mechanical systems. Therefore it is desirable to gain control over the friction process to save non renewable energy sources like petroleum fuels for the future. Another important issue in mechanical devices is the loss of material due to wear. When there is a metal to metal contact, both the surfaces wear off due to high friction. One of the direct methods to reduce friction is to use lubricants. Liquid lubricants reduce friction either by forming additional layers between the contact interfaces or by effectively separating the contacting surfaces. While liquid lubricants are easily introduced to the mechanical parts, solid lubricants have to be coated onto the surface by methods like chemical vapor (CVD) deposition and physical vapor deposition (PVD). Solid lubricants are expected to reduce friction and at the same time protect the interacting surfaces from wear. Many solid lubricants like MoS_2 or graphite have shown to reduce friction to a great extent. These solid lubricants, being chemically inert, are potential candidates for both micro and macro scale applications. Advancements in the fields of nanomechanical and micromechanical devices demand reliable solid lubricants with low adhesion.

Since the isolation of graphene from graphite in 2004 [54] a lot of research work has been carried out to explore its tribological behavior. Graphene has shown to be one of the strongest materials ever tested [41]. Its high chemical inertness, densely packed smooth surface, and the ability to decrease friction are the attracting factors for application as a solid lubricant. Even multilayer graphene is ultrathin and suitable as a solid lubricant for NEMS and MEMS. Bilayer graphene shows an order less magnitude of friction compared to single layer graphene [25]. The potential use of graphene in NEMS and MEMS is limited by the load and roughness of contacting surfaces [78]. Though graphitic surfaces are excellent lubricants, the frictional response for sliding along different directions is not the same at very low loads. With the help of an AFM we explored this anisotropic phenomena which arises due to the symmetry of the graphene surface. By using the method suggested in the

Ref. [12] we could measure the Cartesian components of friction for any arbitrary sliding direction. We finally showed that the friction force is not uniform for all sliding directions. In our experiments we demonstrated that the friction for sliding on graphene or a graphite surface is anisotropic, i.e. the slider experiences different friction forces along different sliding directions. This anisotropic behavior arising from the surface symmetry poses a lower limit for its lubricative action. Graphitic surfaces have six preferred sliding directions which lie along the zig-zag directions of the graphitic surface. Sliding along these directions does not show any deviation in the direction of friction being antiparallel to the sliding direction. Any small deviation in sliding direction from one of the zig-zag directions produces a strong transverse friction force component which tries to pull the slider back to one of the preferred directions. We have found that this anisotropic behavior scales with the sliding distance. Consequences of friction anisotropy are most likely to be encountered in micro/nano scale positioning devices. Mechanical devices designed for accurate positioning purposes, which employ graphene as a lubricant, may encounter errors due to the mechanical parts unable to move freely in all the directions. Our findings on friction anisotropy is supported by the simulation results by Astrid de Wijn [3].

There is a lack of research into the mechanical stability of graphene under high loading conditions. Recent work by Diana Berman et al. [5] reported that solution-processed graphene layers can reduce friction, wear and corrosion rate on sliding steel surfaces in ambient conditions. Here in our work we have successfully grwon large sheets of graphene on Pt(111) and we were successfully imaged the graphene on Pt(111) in contact, noncontact and STM/AFM modes. It is debated that in STM imaging the tip is more likely to go in contact with graphitic surface. But in our High resolution imaging in STM/AFM images the feedback loop is driven by observing the frequency shifts of the cantilever, and we have not observed any significant change in the amplitude of oscillation of the cantilever. This could speak for the cantilever being in out of contact during the STM measurement. More STM

and STM/AFM images can be compared and analyzed in further research works. The average current in the patches differ slightly due to the Moire corrugation. Further careful studies of friction on the polycrystalline patches of graphene is an interesting topic for further research. We have investigated the load bearing strength of graphene at extreme pressures. Simulations carried out by Andreas Klemenz et al. have predicted that graphene can be a very good lubricant even under high pressures. Results from the simulation show that graphene is an excellent coating for achieving low friction and wear. Graphene is tough and shows ultralow friction even at pressures where the substrate starts to undergo plastic deformation due to the continued sliding. However, once the graphene is ruptured it can no longer act as a lubricant and also cannot protect underlying material from wear. Our experimental results of nanoscratch tests on graphene using a diamond coated tip are in good agreement with the simulation results. Since graphene is confirmed to be an excellent lubricant and also to withstand very high loads without breaking, in principle graphene coatings in addition to liquid lubricants in mechanical systems like in automotive engines should lead to a further lowering in friction and wear. There is much more room for further research into graphene's application in surface passivation, and the lowering friction and wear. In future, application of graphene as lubricant in NEMS and MEMS as well as in the large sized machinery parts would be a giant leap in the graphene tribology. However the sizes of contact asperities and the pressure exerted on the asperities in such machinery parts are largely unknown. There is no direct means of measuring these high loading conditions. The possibility of using graphene coating in such tribological systems is still open for further research work. More STM/AFM images of graphene/metal systems can be compared and analyzed in the future works. The average current in the patches of graphene differs slightly depending on Moire corrugation. Therefore one could tune the electronic properties of graphene by its relative orientation on metal substrates. Finally careful studies of friction on the polycrystalline graphene are an interesting topic because the resultant friction due to the individual patches could lead a situation of ultralow

friction.

Errata:

1. page Number.76 : The figure 5.5 has been corrected.

2. page Number.84 (Paragraph.2) : Explanation on extracting exact angular mismatch between graphene and Pt(111) has been added with the reference [81].

ACKNOWLEDGMENTS

My first gratitude must go to my adviser, Prof Roland Bennewitz, for his priceless support and guidance during my research work and also during writing this thesis. He gave me an incredible opportunity of working in his group, and pushed me to improve my understanding as a tribologist. Without his guidance and motivation, none of my work could have been achieved. Additionally, I would also like to thank Dr. Susanne Bennewitz for the care and concern you have shown for me. I would like to thank Prof. Dr. E. Arzt for giving me the opportunity. I would also like to thank INM-Leibniz institute for new Materials, for providing the wonderful working environment and research facilities during my research work. I would sincerely thank my dear colleagues Dr. Florian Hausen, Katrin Brörmann, Suzanna Selzer, Dr. Bianca Bozna, Özgün, Novaf and Johanna Blass for all the help and support they have extended to me. My heartfelt, thanks to Dr. Arnaud Caron who supported me to greater extent during my research work. My special thanks to dear friend Ram Gopal Balijepalli who took care of me from the day I arrived in Germany. My sincere thanks to my teachers Lakshmanaih, Aditya Rao, Dr.Narasihma.A, and Dr. Santosh Kumar Kudtarkar who has greatly influenced me in my academic life. Thanks to my dear cousins Tejaswini and Sashibhushan who always shared my joy and kept me motivated. Special thanks to my dear friends Rajesh Chalasani motivated me to pursue Ph.D . In addition, I thank each and every person who helped me directly or indirectly in my career. Words cannot express how grateful I am to my parents and my sisters Athula Ramesh, Vineetha Prakash and Veena for all their wishes and care towards me. My heartfelt thanks to my in-laws Rangaswamy M.R and Nagamani MR for all their best wishes. Last but not least, I would like to thank my dear wife, Ramya, for always being very much loving and supportive to me throughout this busy and stressful years.

Bibliography

[1] *A Practical Guide to Scanning Probe Microscopy SPM.* www.veeco.com.

[2] TR Albrecht, P Grütter, D Horne, and D Rugar. Frequency modulation detection using high-Q cantilevers for enhanced force microscope sensitivity. *Journal of Applied Physics*, 69(2):668–673, 1991.

[3] SG Balakrishna, Astrid S de Wijn, and Roland Bennewitz. Preferential sliding directions on graphite. *Physical Review B*, 89(24):245440, 2014.

[4] Matthias Batzill. The surface science of graphene: Metal interfaces, CVD synthesis, nanoribbons, chemical modifications, and defects. *Surface Science Reports*, 67(3):83–115, 2012.

[5] Diana Berman, Ali Erdemir, and Anirudha V Sumant. Few layer graphene to reduce wear and friction on sliding steel surfaces. *Carbon*, 54:454–459, 2013.

[6] Bharat Bhushan. Nanotribology and nanomechanics. *Wear*, 259(7):1507–1531, 2005.

[7] Laura B Biedermann, Michael L Bolen, Michael A Capano, Dmitry Zemlyanov, and Ronald G Reifenberger. Insights into few-layer epitaxial graphene growth on 4 H-SiC (000 1^{-}) substrates from STM studies. *Physical Review B*, 79(12): 125411, 2009.

[8] Gerd Binnig, Calvin F Quate, and Ch Gerber. Atomic force microscope. *Physical review letters*, 56(9):930, 1986.

[9] László P Biró and Philippe Lambin. Grain boundaries in graphene grown by chemical vapor deposition. *New Journal of Physics*, 15(3):035024, 2013.

[10] H Bluhm, UD Schwarz, K-P Meyer, and R Wiesendanger. Anisotropy of sliding friction on the triglycine sulfate (010) surface. *Applied Physics A*, 61(5):525–533, 1995.

[11] M Campione and E Fumagalli. Friction anisotropy of the surface of organic crystals and its impact on scanning force microscopy. *Physical Review Letters*, 105(16):166103, 2010.

[12] Marcello Campione, Silvia Trabattoni, and Massimo Moret. Nanoscale mapping of frictional anisotropy. *Tribology Letters*, 45(1):219–224, 2012.

[13] C Julian Chen. *Introduction to scanning tunneling microscopy*. Oxford University Press, 2008.

[14] Johann Coraux, Alpha T N'Diaye, Carsten Busse, and Thomas Michely. Structural coherency of graphene on Ir(111). *Nanoletters*, 8(2):565–570, 2008.

[15] Johann Coraux, Martin Engler, Carsten Busse, Dirk Wall, Niemma Buckanie, Frank-J Meyer Zu Heringdorf, Raoul Van Gastel, Bene Poelsema, Thomas Michely, et al. Growth of graphene on Ir(111). *New Journal of Physics*, 11 (2):023006, 2009.

[16] Paul S Cremer, Xingcai Su, Y Ron Shen, and Gabor A Somorjai. Ethylene hydrogenation on Pt (111) monitored in situ at high pressures using sum frequency generation. *Journal of the American Chemical Society*, 118(12):2942–2949, 1996.

[17] A. S. de Wijn. incommensurability, scaling, and multiplicity of friction in nanocrystals and application to gold nanocrystals on graphite. *Phys. Rev. B*, 86:085429, Aug 2012. doi: 10.1103/PhysRevB.86.085429.

[18] Ulrike Diebold, Lanping Zhang, John F Anderson, and Pawel Mrozek. Surface segregation of silicon in platinum (111). *Journal of Vacuum Science & Technology A*, 14(3):1679–1683, 1996.

[19] Martin Dienwiebel, Gertjan S Verhoeven, Namboodiri Pradeep, Joost WM Frenken, Jennifer A Heimberg, and Henny W Zandbergen. Superlubricity of graphite. *Physical Review Letters*, 92(12):126101, 2004.

[20] C Donnet and A Erdemir. Diamond-like carbon films: a historical overview. *Donnet, C. und A. Erdemir (Herausgeber): Tribology of diamond-like carbon films*, pages 1–10, 2007.

[21] M. Enachescu, D. Schleef, D. F. Ogletree, and M. Salmeron. Integration of point-contact microscopy and atomic-force microscopy: Application to characterization of graphite/Pt(111). *Phys. Rev. B*, 60:16913–16919, Dec 1999. doi: 10.1103/PhysRevB.60.16913.

[22] Y Enomoto and D Tabor. The frictional anisotropy of diamond. *Proceedings of the Royal Society of London. A. Mathematical and Physical Sciences*, 373 (1755):405–417, 1981.

[23] Alexander E. Filippov, Martin Dienwiebel, Joost W. M. Frenken, Joseph Klafter, and Michael Urbakh. Torque and Twist against Superlubricity. *Phys. Rev. Lett.*, 100:046102, Jan 2008. doi: 10.1103/PhysRevLett.100.046102.

[24] T Filleter and R Bennewitz. Structural and frictional properties of graphene films on SiC (0001) studied by atomic force microscopy. *Physical Review B*, 81 (15):155412, 2010.

[25] T Filleter, JL McChesney, A Bostwick, E Rotenberg, KV Emtsev, Th Seyller, K Horn, and R Bennewitz. Friction and dissipation in epitaxial graphene films. *Physical Review Letters*, 102(8):086102, 2009.

[26] Enrico Gnecco, Oscar Y Fajardo, Carlos M Pina, and Juan J Mazo. Anisotropy Effects in Atomic-Scale Friction. *Tribology Letters*, 48(1):33–39, 2012.

[27] JT Grant and TW Haas. A study of Ru (0001) and Rh (111) surfaces using LEED and Auger electron spectroscopy. *Surface Science*, 21(1):76–85, 1970.

[28] Alexander Grüneis, Kurt Kummer, and Denis V Vyalikh. Dynamics of graphene growth on a metal surface: a time-dependent photoemission study. *New Journal of Physics*, 11(7):073050, 2009.

[29] S. Hagstrom, H. B. Lyon, and G. A. Somorjai. Surface Structures on the Clean Platinum (100) Surface. *Phys. Rev. Lett.*, 15:491–493, Sep 1965. doi: 10.1103/PhysRevLett.15.491.

[30] JA Harrison, CT White, RJ Colton, and DW Brenner. Molecular-dynamics simulations of atomic-scale friction of diamond surfaces. *Physical Review B*, 46 (15):9700, 1992.

[31] Motohisa Hirano and Kazumasa Shinjo. Superlubricity and frictional anisotropy. *Wear*, 168(1):121–125, 1993.

[32] Motohisa Hirano, Kazumasa Shinjo, Reizo Kaneko, and Yoshitada Murata. Anisotropy of frictional forces in muscovite mica. *Physical Review Letters*, 67 (19):2642, 1991.

[33] Hendrik Hölscher, André Schirmeisen, and Udo D Schwarz. Principles of atomic friction: from sticking atoms to superlubric sliding. *Philosophical Transactions of the Royal Society A: Mathematical, Physical and Engineering Sciences*, 366 (1869):1383–1404, 2008.

[34] Vivek Kalihari, EB Tadmor, Greg Haugstad, and C Daniel Frisbie. Grain orientation mapping of polycrystalline organic semiconductor films by transverse shear microscopy. *Advanced Materials*, 20(21):4033–4039, 2008.

[35] J Kerssemakers and J Th M De Hosson. Influence of spring stiffness and anisotropy on stick-slip atomic force microscopy imaging. *Journal of Applied Physics*, 80(2):623–632, 1996.

[36] Andreas Klemenz, Lars Pastewka, Soorali Ganeshamurthy Balakrishna, Arnaud Caron, Roland Bennewitz, and Michael Moseler. Atomic Scale Mechanisms of Friction Reduction and Wear Protection by Graphene. *Nanoletters*, 2014.

[37] A. R. Konicek, D. S. Grierson, P. U. P. A. Gilbert, W. G. Sawyer, A. V. Sumant, and R. W. Carpick. Origin of Ultralow Friction and Wear in Ultrananocrystalline Diamond. *Phys. Rev. Lett.*, 100:235502, Jun 2008. doi: 10.1103/PhysRevLett.100.235502.

[38] Pamela T Korda, Michael B Taylor, and David G Grier. Kinetically locked-in colloidal transport in an array of optical tweezers. *Physical Review Letters*, 89 (12):128301, 2002.

[39] TA Land, Th Michely, RJ Behm, JC Hemminger, and G Comsa. STM investigation of single layer graphite structures produced on Pt (111) by hydrocarbon decomposition. *Surface Science*, 264(3):261–270, 1992.

[40] B Lang. A LEED study of the deposition of carbon on platinum crystal surfaces. *Surface Science*, 53(1):317–329, 1975.

[41] Changgu Lee, Xiaoding Wei, Jeffrey W Kysar, and James Hone. Measurement of the elastic properties and intrinsic strength of monolayer graphene. *Science*, 321(5887):385–388, 2008.

[42] Changgu Lee, Xiaoding Wei, Jeffrey W Kysar, and James Hone. Measurement of the elastic properties and intrinsic strength of monolayer graphene. *Science*, 321(5887):385–388, 2008.

[43] Hyunsoo Lee, Naesung Lee, Yongho Seo, Jonghwa Eom, and SangWook Lee. Comparison of frictional forces on graphene and graphite. *Nanotechnology*, 20 (32):325701, 2009.

[44] M. Liley, D. Gourdon, D. Stamou, U. Meseth, T. M. Fischer, C. Lautz, H. Stahlberg, H. Vogel, N. A. Burnham, and C. Duschl. Friction Anisotropy

and Asymmetry of a Compliant Monolayer Induced by a Small Molecular Tilt. *Science*, 280(5361):273–275, 1998. doi: 10.1126/science.280.5361.273.

[45] Li-Yu Lin, Dae-Eun Kim, Whan-Kyun Kim, and Seong-Chan Jun. Friction and wear characteristics of multi-layer graphene films investigated by atomic force microscopy. *Surface and Coatings Technology*, 205(20):4864–4869, 2011.

[46] E Loginova, NC Bartelt, PJ Feibelman, and KF McCarty. Factors influencing graphene growth on metal surfaces. *New Journal of Physics*, 11(6):063046, 2009.

[47] D Marchetto, C Held, F Hausen, F Wählisch, M Dienwiebel, and R Bennewitz. Friction and wear on single-layer epitaxial graphene in multi-asperity contacts. *Tribology Letters*, 48(1):77–82, 2012.

[48] Cristina Martin-Olmos, Haider Imad Rasool, Bruce H Weiller, and James K Gimzewski. Graphene MEMS: AFM probe performance improvement. *ACS nano*, 7(5):4164–4170, 2013.

[49] C Mathew Mate, Gary M McClelland, Ragnar Erlandsson, and Shirley Chiang. Atomic-scale friction of a tungsten tip on a graphite surface. In *Scanning Tunneling Microscopy*, pages 226–229. Springer, 1993.

[50] E. Meyer and Ernst Meyer. *Nanoscience: Friction and Rheology on the Nanometer Scale*. World Scientific, 1998. ISBN 9789810225629.

[51] E Meyer, H Heinzelmann, P Grütter, Th Jung, H-R Hidber, H Rudin, and H-J Güntherodt. Atomic force microscopy for the study of tribology and adhesion. *Thin Solid Films*, 181(1):527–544, 1989.

[52] Gerhard Meyer and Nabil M Amer. Novel optical approach to atomic force microscopy. *Applied Physics Letters*, 53(12):1045–1047, 1988.

[53] RG Musket, W McLean, C A_ Colmenares, DM Makowiecki, and WJ Siekhaus.

Preparation of atomically clean surfaces of selected elements: a review. *Applications of Surface Science*, 10(2):143–207, 1982.

[54] Kostya S Novoselov, Andre K Geim, SV Morozov, D Jiang, Y_ Zhang, SV Dubonos, IV Grigorieva, and AA Firsov. Electric field effect in atomically thin carbon films. *Science*, 306(5696):666–669, 2004.

[55] KSA Novoselov, Andre K Geim, SVb Morozov, Da Jiang, MI Katsnelson IV Grigorieva, SV Dubonos, and AA Firsov. Two-dimensional gas of massless Dirac fermions in graphene. *Nature*, 438(7065):197–200, 2005.

[56] R. M. Overney, H. Takano, M. Fujihira, W. Paulus, and H. Ringsdorf. Anisotropy in friction and molecular stick-slip motion. *Phys. Rev. Lett.*, 72:3546–3549, May 1994. doi: 10.1103/PhysRevLett.72.3546.

[57] Jeong Young Park, DF Ogletree, M Salmeron, RA Ribeiro, PC Canfield, CJ Jenks, and PA Thiel. High frictional anisotropy of periodic and aperiodic directions on a quasicrystal surface. *Science*, 309(5739):1354–1356, 2005.

[58] Natalia Starostina Paul West. *A Guide to AFM Image Artifacts*. Pacific Nanotechnology, Inc.

[59] Oleksiy Penkov, Hae-Jin Kim, Hyun-Joon Kim, and Dae-Eun Kim. Tribology of graphene: a review. *International journal of precision engineering and manufacturing*, 15(3):577–585, 2014.

[60] Marin Petrović, I Šrut Rakić, Sven Runte, Carsten Busse, JT Sadowski, Predrag Lazić, Ivo Pletikosić, Z-H Pan, Milorad Milun, Petar Pervan, et al. The mechanism of caesium intercalation of graphene. *Nature Communications*, 4, 2013.

[61] VL Popov and JAT Gray. Prandtl-Tomlinson model: History and applications in friction, plasticity, and nanotechnologies. *ZAMM-Journal of Applied Mathematics and Mechanics/Zeitschrift für Angewandte Mathematik und Mechanik*, 92(9):683–708, 2012.

[62] L. Prandtl. Ein Gedankenmodell zur kinetischen Theorie der festen Körper. *ZAMM - Journal of Applied Mathematics and Mechanics / Zeitschrift für Angewandte Mathematik und Mechanik*, 8(2):85–106, 1928. ISSN 1521-4001. doi: 10.1002/zamm.19280080202.

[63] Ernest Rabinowicz. Direction of the friction force. *Nature*, 179:1073, 1957.

[64] M. V. Rastei, B. Heinrich, and J. L. Gallani. Puckering Stick-Slip Friction Induced by a Sliding Nanoscale Contact. *Phys. Rev. Lett.*, 111:084301, Aug 2013. doi: 10.1103/PhysRevLett.111.084301.

[65] Ju-Ai Ruan and Bharat Bhushan. Atomic-scale and microscale friction studies of graphite and diamond using friction force microscopy. *Journal of applied physics*, 76(9):5022–5035, 1994.

[66] Ju-Ai Ruan and Bharat Bhushan. Frictional behavior of highly oriented pyrolytic graphite. *Journal of Applied Physics*, 76(12):8117–8120, 1994.

[67] M. Salmeron and G. A. Somorjai. Desorption, decomposition, and deuterium exchange reactions of unsaturated hydrocarbons (ethylene, acetylene, propylene, and butenes) on the platinum (111) crystal face. *The Journal of Physical Chemistry*, 86(3):341–350, 1982.

[68] Naruo Sasaki, Katsuyoshi Kobayashi, and Masaru Tsukada. Atomic-scale friction image of graphite in atomic-force microscopy. *Phys. Rev. B*, 54:2138–2149, Jul 1996. doi: 10.1103/PhysRevB.54.2138.

[69] Robert H Savage. Graphite lubrication. *Journal of Applied Physics*, 19(1):1–10, 1948.

[70] Paul E. Sheehan and Charles M. Lieber. Nanotribology and Nanofabrication of MoO 3 by Atomic Force Microscopy. *Science*, 272(5265):1158–1161, 1996. doi: 10.1126/science.272.5265.1158.

[71] Hitoshi Shindo, Kozo Shitagami, Takashi Sugai, and Kondo Sei-ichi. Evidence of the contribution of molecular orientations on the surface force friction of alkaline earth sulfate crystals. *Phys. Chem. Chem. Phys.*, 1(7):1597–1600, 1999.

[72] David Speer, Ralf Eichhorn, and Peter Reimann. Directing Brownian motion on a periodic surface. *Physical Review Letters*, 102(12):124101, 2009.

[73] Pascal Steiner, Raphael Roth, Enrico Gnecco, Alexis Baratoff, and Ernst Meyer. Angular dependence of static and kinetic friction on alkali halide surfaces. *Physical Review B*, 82(20):205417, 2010.

[74] GA Tomlinson. A molecular theory of friction. *The London, Edinburgh, and Dublin philosophical magazine and journal of science*, 7(46):905–939, 1929.

[75] A Ya Tontegode. Carbon on transition metal surfaces. *Progress in Surface Science*, 38(3):201–429, 1991.

[76] M.A. VanHove, W.H. Weinberg, and C.M. Chan. *Low-Energy Electron Diffraction: Experiment, Theory and Surface Structure Determination*. Springer Series in Surface Sciences. Springer Berlin Heidelberg, 2011. ISBN 9783642827235.

[77] Gertjan S Verhoeven, Martin Dienwiebel, and Joost WM Frenken. Model calculations of superlubricity of graphite. *Physical Review B*, 70(16):165418, 2004.

[78] Felix Wählisch, Judith Hoth, Christian Held, Thomas Seyller, and Roland Bennewitz. Friction and atomic-layer-scale wear of graphitic lubricants on SiC (0001) in dry sliding. *Wear*, 300(1):78–81, 2013.

[79] Alfred J Weymouth, Daniel Meuer, Pingo Mutombo, Thorsten Wutscher, Martin Ondracek, Pavel Jelinek, and Franz J Giessibl. Atomic structure affects the directional dependence of friction. *Physical Review Letters*, 111(12):126103, 2013.

[80] Joost Wintterlin and M-L Bocquet. Graphene on metal surfaces. *Surface Science*, 603(10):1841–1852, 2009.

[81] Patrick Zeller and Sebastian Günther. What are the possible moiré patterns of graphene on hexagonally packed surfaces? Universal solution for hexagonal coincidence lattices, derived by a geometric construction. *New Journal of Physics*, 16(8):083028, 2014.

[82] Hu Zi-Pu, DF Ogletree, MA Van Hove, and GA Somorjai. LEED theory for incommensurate overlayers: Application to graphite on Pt (111). *Surface Science*, 180(2):433–459, 1987.